

Review

A Review of Optical Sensors in CMOS

Rodrigo Gounella ¹, Gabriel M. Ferreira ^{2,3,4}, Marcio L. M. Amorim ¹, João Navarro Soares, Jr. ¹
and João Paulo Carmo ^{1,*}

¹ Group of Metamaterials Microwaves and Optics (GMeta), Department of Electrical Engineering (SEL), University of São Paulo (USP), Avenida Trabalhador São-Carlense, Nr. 400, Parque Industrial Arnold Schimidt, São Carlos CEP 13566-590, SP, Brazil; rodrigogounella@usp.br (R.G.); marciolma@usp.br (M.L.M.A.); navarro@sc.usp.br (J.N.S.J.)

² Microelectromechanical Systems Research Unit (CMEMS-UMinho), School of Engineering, Campus de Azurém, University of Minho, 4800-058 Guimarães, Portugal; id10786@alunos.uminho.pt

³ LABBELS—Associate Laboratory, 4800-122 Braga, Portugal

⁴ International Iberian Nanotechnology Laboratory, INL, 4715-330 Braga, Portugal

* Correspondence: jcarmo@sc.usp.br

Abstract: This paper presents an overview of silicon-based optical sensors for the measurement of light in the visible spectrum range. The review is focused on sensors based on CMOS (complementary metal-oxide semiconductor) technology due to the high availability, low cost, ease of prototyping, and well-established fabrication processes. CMOS technology allows integration with the CMOS readout and control electronics in the same microdevice, featuring high-volume fabrication with high-reproducibility and low-cost. This review starts with an explanation of the phenomena behind opto-electronic transduction. It also presents and describes the most common components responsible for optical transduction, readout electronics, and their main characteristics. This review finishes with the presentation of selected applications to grasp where and how these sensors can be used.

Keywords: solid-state optical sensor; CMOS; optical transduction; photodetector; readout electronics



Citation: Gounella, R.; Ferreira, G.M.; Amorim, M.L.M.; Soares, J.N., Jr.; Carmo, J.P. A Review of Optical Sensors in CMOS. *Electronics* **2024**, *13*, 691. <https://doi.org/10.3390/electronics13040691>

Academic Editor:
Esteban Tlelo-Cuautle

Received: 24 November 2023

Revised: 27 January 2024

Accepted: 2 February 2024

Published: 8 February 2024



Copyright: © 2024 by the authors. Licensee MDPI, Basel, Switzerland. This article is an open access article distributed under the terms and conditions of the Creative Commons Attribution (CC BY) license (<https://creativecommons.org/licenses/by/4.0/>).

1. Introduction

Microsystems are widely found on everyday life thanks to microfabrication techniques [1–4]. The need for new applications resulted in the development of compact wireless sensors of very small sizes and with minimal power consumption [5,6], object tagging and components for chain fabrication facilities [7,8], and micropowering with silicon-compatible microbatteries [9] and photonic applications [10,11]. However, and despite fascinating microsystem applications, among the most challenging applications are those targeted to detect [12] and/or manipulate [13] light. Light is, without any shadow of doubt, the most fascinating phenomenon in nature because it affects all aspects of physics of the universe and of living creatures [14] and, paradoxically, even when it is not present [15]. A detailed search for applications of optical microsystems makes it possible to conclude that optical detection is the main physical mechanism. Moreover, silicon is widely used to build photodetectors for the visible region of the electromagnetic spectrum [16]. This fact has been observed in recent decades with the mass application of CMOS (complementary metal-oxide semiconductor) technology in consumer electronics and image acquisition systems [17], and successive improvements to the respective manufacturing processes. This paper presents a comprehensive review of optical sensors in CMOS, which starts with an explanation of opto-electronic transduction to allow the reader to understand the basis of this review. Opto-electronic transduction results in the creation of electrons (and holes also), which produces a photogenerated electrical current [18] that must be converted into a voltage signal for further conversion to the digital domain. New concepts designed to overcome the limitations of low-energy photons and to improve the quantum efficiency of silicon photodetectors are presented herein. It is also relevant to know which

options are technologically available for conversion; thus, the different types of transducers and architectures of readout electronics and the respective features and limitations are also described. This paper finishes with selected applications of optical sensors in CMOS technology developed by researchers from our present and past research groups. CMOS technology was selected due to the high potential for miniaturization achieved through the integration of optical transducers and readout electronics in the same microdevice, and the high availability of foundries and processes. Figure 1 illustrates a flowchart with the structure of this review. The arrows show the dependencies of several sections. The last section, with the applications, requires prior understanding and knowledge of the different architectures of photoconversion.

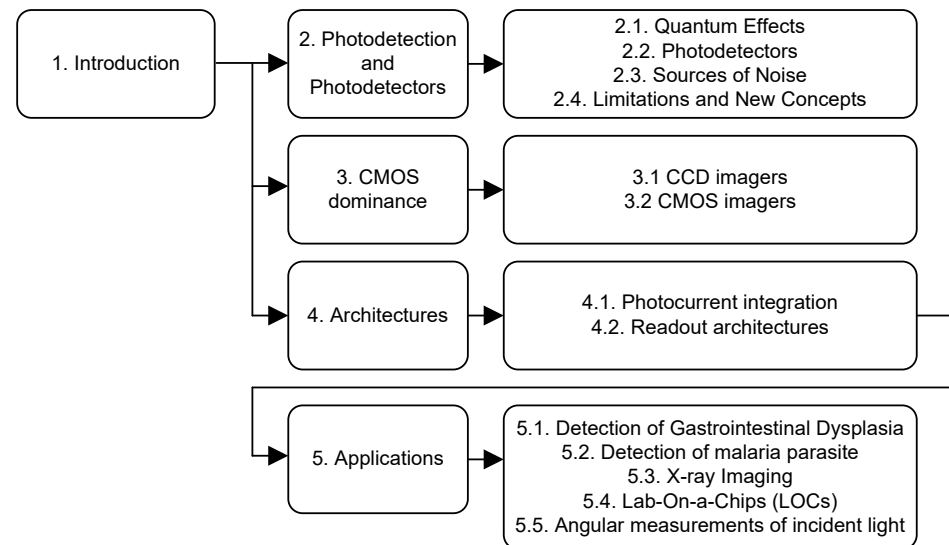


Figure 1. Flowchart with the structure of this review and the dependencies of the sections.

2. Photodetection and Photodetectors

2.1. Quantum Effects

The photonic penetration depth on silicon, i.e., the light absorption, depends on the wavelength. This means that the longer the wavelength λ [m] of a photon, the lower is its energy, and the further it can delve into silicon [18]. Figure 2a illustrates a silicon cross-section to demonstrate electron-hole pair creation, when the energy of an incident photon increases above the bandgap energy E_{gap} [eV] of a semiconductor material [19]. The bandgap energy of silicon is ≈ 1.12 eV. The higher the energy, the lower the wavelength. The electron-hole collection that produces a photo-current is improved when a PN junction is used. Figure 2b illustrates such a junction. The pairs will be collected within the depletion region due to the presence of an inherent electrical field V_{bi} [V] in the PN junction [19]. The pairs formed beyond the depletion zone may recombine again prior to crossing the depletion barrier. These losses decrease the quantum efficiency of the photodetector.

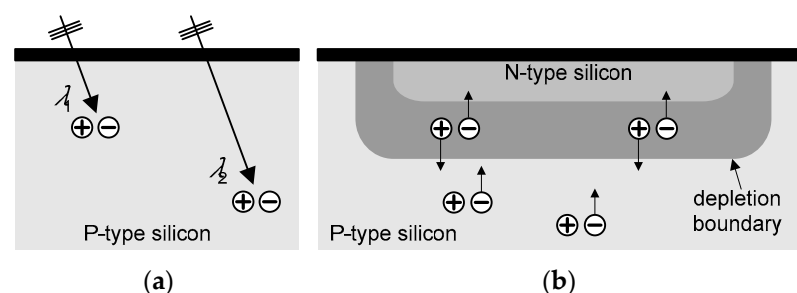


Figure 2. (a) Illustration of electron-hole pair generation with different wavelengths, with $\lambda_1 < \lambda_2$. (b) Illustration electron-hole pair collection in a PN junction [19].

Figure 3 presents the optical absorption coefficient [1/cm] and the absorption depth [cm] of silicon as a function of the wavelength, where it can be observed that how high the wavelength λ [m] is. It can be observed that the lower the absorption, the deeper the penetration [18]. Figure 3 also shows the boundaries of the visible range of the electromagnetic spectrum between 390 nm and 760 nm [14]. This behavior is due to the indirect gap material being silicon; thus, the absorption coefficient exhibits a comparably slight value, meaning that the photons are gradually absorbed by the material.

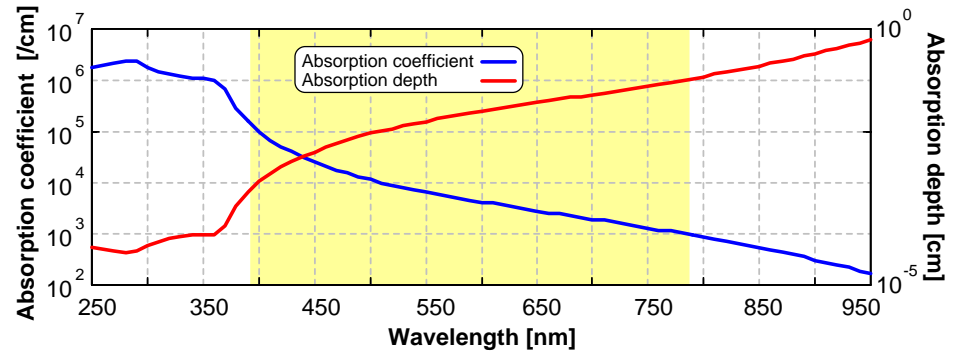


Figure 3. The absorption coefficient [1/cm] (blue line) and the absorption depth [cm] (red line) of silicon [18], both represented on a logarithmic scale. The boundary of the visible range of the electromagnetic spectrum is highlighted in yellow [14].

Silicon photodetectors can create photogenerated currents for impinging light with wavelengths across the complete visible range. The produced photocurrent is proportional to the intensity of the incident light [19–21] and is given by [21]:

$$I_{ph} = \frac{e \times QE \times \lambda \times P_i}{hc} = \frac{e \times QE \times P_i}{h\nu}, \tag{1}$$

where I_{ph} [A] is the photocurrent, e [C] is the elementary charge, λ [m] is the wavelength of the incident light, QE [%] is the quantum efficiency, P_i [W] is the incident optical power, h [J.Hz⁻¹] is Planck’s constant, and c [m.s⁻¹] is the velocity of light in a vacuum. The quantity $E = hc/\lambda = h.\nu$ [eV] is the energy of a photon and ν [Hz] is the frequency of the photons. Formally, the quantum efficiency is determined by the ratio of the generated electrons N_e to the incident photons N_{ph} within the photodetector [21]:

$$QE = \frac{N_e}{N_{ph}} = \frac{\left(\frac{I_{ph}}{e}\right)}{\left(\frac{P_i}{h\nu}\right)} = R \times \left(\frac{h\nu}{e}\right), \tag{2}$$

where R [A/W] is the responsivity of the photodetector. Responsivity is very important because it relates the generated photocurrent I_{ph} [A] with the impinged optical power P_i [W], e.g., $R = I_{ph}/P_i$ [A/W]. Hence, after acquiring the photocurrents, the primary physical quantity that was obtained is the responsivity. Subsequently, the quantum efficiency is derived from Equation (2).

It is straightforward to obtain experimentally the responsivity and the quantum efficiency [12,22]. These kinds of experiments require setups with an optical source. Figure 4 shows an example of an experimental setup used by Costa et al. to obtain the responsivity and the quantum efficiency of photodiodes [12]. A 250 W quartz tungsten halogen lamp from Oriel is widely used as an optical source. A monochromator, for example, the Newport model CornerStone 130, is also required to sweep the wavelength of the light across the visible range. An optical fiber is needed to couple the light to the photodetectors, which can be a Newport model Standard Grade FS Fiber Optic. For example, the Keithley 487 picoammeter measures the photocurrents produced by the photodiodes. Finally, a commercial photodiode with a known spectral response, such as the Hammamatsu S1336-5BQ, can

serve as a benchmark to offset the light's spectral characteristics at the monochromator output. Typically, responsivity is a readily available parameter in commercial photodetector datasheets. The photocurrent I_{ph} [A] of the photodetector under characterization must be measured at each wavelength. The photocurrent of the commercial photodiode $I_{commercial}$ [A] must also be acquired to compensate the spectral signature of the light at the output of monochromator. The responsivity R_{PD} [A/W] of each photodiode is calculated according [21]:

$$R_{PD,i} = f(\lambda) \times I_{PD,i} = \left(\frac{R_{commercial}}{I_{commercial}} \right) \times I_{PD,i}, \quad (3)$$

where $f(\lambda)$ is a function used in spectral compensation. Also required is the use of a pinhole mounted on top of the commercial photodetector, with an aperture equal to the active area of the photodetector under examination. The pinhole ensures that the illuminated area on both photodetectors is the same.

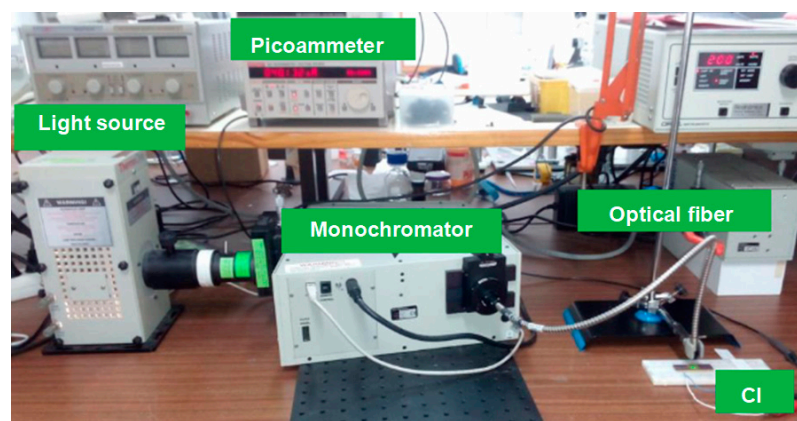


Figure 4. Optical setup for the spectral analysis of photodetectors. This setup was used by Costa et al. to obtain the responsivity and the quantum efficiency of photodiodes [12].

The example in Figure 5 shows the responsivity (red trace) and the quantum efficiency (blue trace) of a photodiode, which were obtained by applying Equations (1) and (2) to the measured photocurrents. This photodiode was implemented in CMOS 0.7 μm from the on semiconductor (former Alcatel-MIETEC) [12]. A decrease in the responsivity before the energy of photons becoming lower than the gap energy of silicon can be also observed in Figure 5. This is due to the decrease of absorption in the silicon increasing the penetration depth and leading to distribution over a large depth of the photo-generated electron–hole pairs. As a consequence, the collection of all of these carriers to generate a photocurrent is difficult. Therefore, it is for this reason that the low responsivity is due to the recombination of the generated electron–hole pairs.

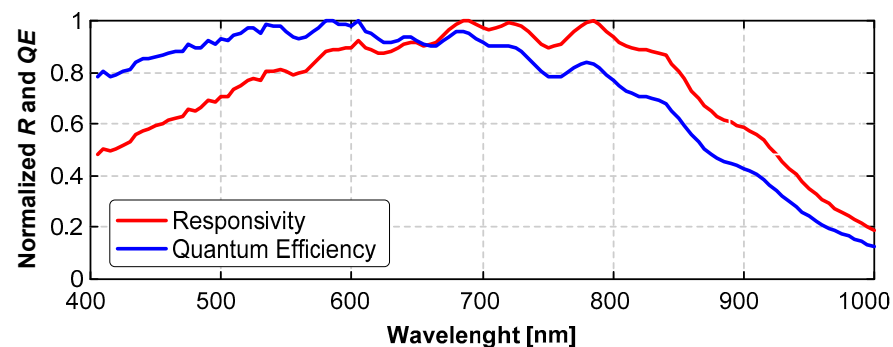


Figure 5. Measured responsivity (red trace) and quantum efficiency (blue trace) of a N^+ /P-sub junction photodiode implemented in CMOS 0.7 μm from the on semiconductor with an active area of $94 \mu\text{m} \times 94 \mu\text{m}$ [12].

2.2. Photodetectors

There exist primarily two types of photodetector configuration within CMOS technology utilizing N-well: the photodiode and the phototransistor [22,23]. The photogates can also be used, but this depends on the characteristics of the selected process, e.g., the gate material must be highly transmissive in optical terms, meaning that materials such as metals or silicon compounds must be avoided [24,25]. Avalanche photodiodes can also be used, but these photodetectors do not allow the implementation of electronic circuits in the same microdevice due to the high biasing voltages in the order of dozens of Volts [26]. For these reasons, this section discusses only photodiodes and the phototransistor structures since they are the most suitable for light detection in the visible spectral range and, at the same time, these photodetectors can be integrated with the readout electronics in the same microdevice and in the same substrate [27].

Figure 6a illustrates three types of vertical photodiodes suitable for fabrication in standard N-well CMOS processes: photodiodes using the N-well/P-sub, P⁺/N-well, and N⁺/P-sub junctions [28]. The operation of these photodiodes is similar, differing only in terms of junction depth. However, in a standard CMOS process, the depth of the PN junction is fully defined and cannot be altered [29]. So, the responsivity, the quantum efficiency, and the dark current differ according to each CMOS process. Each CMOS process presents different junction depths and dopant concentration. This results in photodiodes with different characteristics, as demonstrated through simulations in [30]. Furthermore, Ferreira et al. [30] also demonstrated the interference effect of the oxide layers on top of the photodetectors inherent to a standard CMOS process in terms of the performance of CMOS photodetectors. These factors notably impact the curves of quantum efficiency, encompassing the quantity of layers, their thickness, and the refractive index of the materials used. Additionally, variations in manufacturing techniques between different foundries can result in slight deviations in fabrication parameters, thereby yielding distinct performances of the photodiodes [30].

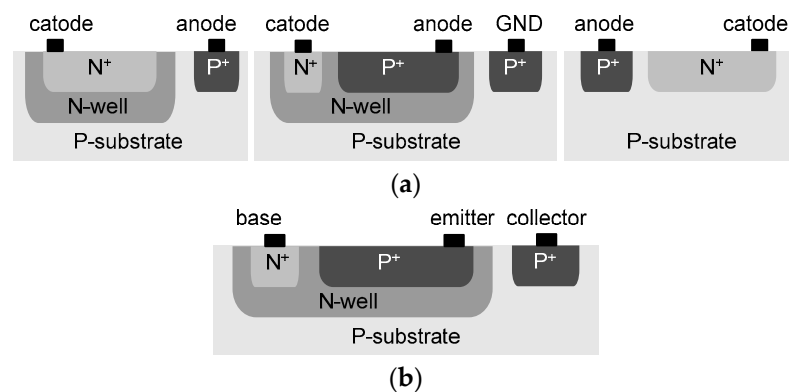


Figure 6. (a) The three types of possible vertical photodiodes; from left to right: N-well/P-sub, P⁺/N-well, and N⁺/P-sub junctions [28]. (b) Cross-section of a vertical junction phototransistor [23].

Theoretically, from the vertical photodiodes available in a CMOS process, the N⁺/P-sub junction photodiode is the one that provides the best possible quantum efficiency in the visible spectral range and, at the same time, yielding the highest possible fill factor [28] since a deep N-well is not required in architectures with several photodetectors (also known as pixels). However, for different CMOS processes, the dopant concentration and the junction's capacitance have different contributions to the photodiode's structure. For the 0.7 μm CMOS process, Minas et al. concluded that the N⁺/P-sub junction was the one that presented the highest quantum efficiency in the visible spectrum; because of varying doping concentrations between the N and P sides, the depletion on the P side extends further [31]. However, Joon Huang Chuah et al. [32] and Gözen Köklü et al. [33] demonstrated that the N-well/P-sub and P⁺/N-well junctions made it possible to obtain a

higher quantum efficiency for the 0.35 μm and the 0.18 μm CMOS processes, respectively, in the visible region of the optical spectrum, due to the larger depletion region available against the N^+/P -sub junction photodiode [32,33].

CMOS technology with an N-well implant also allows the implementation of bipolar phototransistors with lateral and vertical junctions [23,29]. Both structures use the photoelectric effect to convert photons to electron–hole pairs. These electron–hole pairs are separated and recollected, using a reversed biased PN junction very close to a directly biased PN junction. The incident light in the reversed junction, e.g., in the collector–base junction, originates an electrical current proportional to the incident light. This current enters in base region and is multiplied by a β factor. This β factor is the gain current of the transistor, higher than the unity, making the quantum efficiency of the phototransistor higher than 100%. The phototransistor based on a lateral-junction bipolar transistor provides a higher β factor than the vertical-junction bipolar transistor, but presents a complex structure and large device-to-device variations, both of which can be detrimental to array-type detector implementation and performance [23]. A phototransistor based on a vertical junction bipolar transistor provides high compactness and moderate gain and speed [23]. It is feasible to obtain gains of over one hundred with this structure, using a special layout [23]. Figure 6b shows the cross-section of a vertical-junction bipolar phototransistor, using the junctions P^+/N -well and P -sub.

2.3. Sources of Noise

There are other physical phenomena associated with the carrier-generation process previously explained. The primary and foremost origin of noise in photodetectors arises from the dark current, e.g., a current present within a photodiode in the absence of incident optical radiation [22,34]. This current may arise due to the saturation current, which results from minority carriers (like electrons in the P-type region and holes in the N-type region) diffusing at the edges of the depletion zone. Additionally, thermal excitation can generate minority charge carriers. Therefore, a single measurement at the start of the experiment may not be adequate [22]. It is common to use of a dark current compensation circuit, using a photodetector completely covered with metal [22,35]. The experiments conducted by Rocha et al. [34] have proven a reduction in the mean values of dark current when placing microlenses on top of N^+/P -sub photodiodes. However, the reasons behind this reduction are not yet fully understood [34].

Thermal noise is due to the thermal agitation of electrons within a resistance, with a power spectral density given by [36]:

$$S_v(f) = \overline{v_n^2} = 4kTR \text{ [V}^2/\text{Hz]}, \quad (4)$$

where k [$\text{J}\cdot\text{K}^{-1}$] is Boltzmann's constant, T [K] is the absolute temperature, and R [Ω] is the resistance. The parasitic resistances of electrical interconnections to the photodetector are sources of thermal noise [36]. Moreover, the reset switch (when it is switched) on can be considered a resistance and the amplifier connected to the photodetector can also contribute to the total amount of thermal noise [37].

The $1/f$ noise appears on readout electronics, especially on the in-pixel source-followers normally present on a CMOS imager [38,39]. This noise is due to the lattice defects at the interface of the Si-SiO₂ channel of the MOSFETs. The power spectral density of this noise is proportional to $1/f$ [39]. This noise can be reduced with a correlated double sampling (CDS) technique [38,39], as long as the interval between the two samples is short enough to make the $1/f$ noise behave as a simple offset.

Photon shot noise occurs due to the unpredictable arrival of photons. As a result, uncertainties in the sensor's output arise from random fluctuations during the photon capture process by the photodiode [40]. Photon shot noise can be modeled by a Poisson random process and, unlike other noise sources on photodetectors, photon shot noise is a unique noise which has a constant relationship to the illumination level.

2.4. Limitations and New Concepts

Photodetection with silicon devices faces several limitations, e.g., the diffraction and refraction of light on the surface of the active media and low-energy photons. The quantum efficiency can be improved by overcoming the first limiting factor [41]. Combining metasurfaces with photodetectors has the potential to enhance the interaction of the light with the matter and, at the same time, to manipulate and resolve other factors besides the amplitude such as phase, frequency, and polarization at the pixel level [42,43]. Such metasurfaces are made of arrays of structures with dimensions smaller than the wavelength of interest [41,44]. These nanometric structures are known as optical antennas [45]. This means that the subwavelength nanostructures must be capable of manipulating the light at the subwavelength scale [41,44]. Metasurfaces are inherently planar structures, being very easy to fabricate with planar fabrication tools and processes, such as those found in the microsystems industry [44,46]. Moreover, planar structures are more cost-effective when compared with the fabrication of tridimensional structures [44,47]. According to Li et al. [41] and Bharadwaj et al. [48], the application of metasurfaces in photodetection can be categorized as near-field scattering, resonant detection, and far-field scattering. Near-field scattering in metasurfaces confines the light in their vicinity, enhancing the interaction with the matter and promoting the transduction of photons into electric signals, e.g., enhancing the effective responsivity at the wavelengths of interest [41,45]. In resonant detection, the light impinging the metasurface couples into the resonant modes of nanostructured semiconductors, being efficiently absorbed because the interaction of light with the matter is enhanced by the resonance interactions [41,49]. Moreover, the resonant modes coupled into nanostructured semiconductors can dramatically enhance the photoresponse and enable wavelength and polarization selectivity [41,49]. Arrays of optical antennas are employed to selectively transmit the impinging light towards the far-field, working as optical devices such as optical filters or polarizers, among others [41]. The fabrication of these types of metasurface filters are compatible with CMOS microdevices because they can be integrated [21,30,34] or even simply positioned and placed after the fabrication of the microdevice [50]. Pixel-size reduction normally results in a reduction in the total dark current. The pixel dark current also reduces in accordance with the process of technology shrinkage [51]. Moreover, shrinking the pixel size also results in a reduction in the sensitivity under low-light conditions [51]. It has been demonstrated that the photoconversion reduction is higher than the dark current reduction when the pixel size decreases [51]. In conclusion, pixel reduction is something that, in addition to size, normally cannot be controlled without combining new approaches offered by physics. Optical antennas combined with the reduction in pixel size overcome the previous limitation by improving the “signal-to-noise” ratio [41]. This happens because the photodetector’s dark current is reduced to a fraction of that observed on a conventional photodetector and, at the same time, the optical antenna on a pixel significantly improves the absorption of the photodetector [41].

Another way to overcome the diffraction and refraction of light in order to improve the optic absorption is increasing the photogeneration of electron–hole pairs by integrating nanostructures onto electronic devices [52,53]. It has been widely documented that nanostructures on top of polysilicon gate terminals of MOSFETs have great application potential for a wide range of applications, such as in chemical [54] and physical [55] sensing, owing to their unique chemical and physical properties as well as electronic device fabrication compatibilities [55]. A layer of silicon nanograss on top of the polysilicon gate of phototransistors can improve the absorption of light and promote optical sensitivity proportional to the quantity $(V_{gs} - V_{th})^{-1}$, where V_{th} is the threshold voltage of the active device and V_{gs} is the gate-source voltage [55].

Traditional approaches to optical detection based on the phenomenon of direct photogeneration of electron–hole pairs on bulk silicon face an absolute physical limit imposed by the energy of photons, where their energy decreases with the increase in wavelength [21]. The impinging photons cease to create electron–hole pairs at a certain point with enough

low energy. Therefore, the detection of low-energy photons, for example, at telecommunication infrared bands of 1300 nm and 1550 nm, is a challenge with silicon detectors and alternative detection schemes are required. One of the most popular detection schemes for low-energy photons is hot-electron photodetection [56]. This promising technique takes advantage of the unique properties of plasmonic materials, typically metals such as gold or silver, to amplify and concentrate electromagnetic fields at the nanoscale [56,57]. When a metal nanoparticle is exposed to light, it can support localized surface plasmon resonances (LSPRs). LSPR occurs when the frequency of incident photons matches the oscillation frequency of the conduction electrons in the metal, leading to enhanced electromagnetic fields around the nanoparticle [41,56]. Low-energy photons, which may not have sufficient energy to excite electrons across the bandgap of traditional semiconductor materials, can still be absorbed by plasmonic nanoparticles [56,58]. The enhanced electromagnetic fields near the nanoparticle surface enable the transfer of energy from plasmons to free electrons in the metal and create excited electrons with energies lower than the metal's work function [56,58]. These high-energy, or hot electrons are now free to move within the metal and can be extracted for further use [59]. Plasmonic hot electrons can be collected and utilized in a photodetector setup [58]. This can involve placing a semiconductor material in close proximity to the plasmonic structure, allowing the generated hot electrons to transfer into the semiconductor, where they contribute to a measurable photocurrent [41,56–59]. Plasmonic materials can be engineered to exhibit tunable LSPR frequencies, enabling the optimization of the photodetection process for specific wavelengths or energy ranges. This tunability enhances the sensitivity of the detector to low-energy photons [41,58]. By leveraging plasmonic hot electrons, researchers can create photodetectors that are capable of efficiently capturing and converting the energy from low-energy photons into electrical signals, opening up new possibilities for applications in fields such as photovoltaics, sensing, and imaging [59]. Recent demonstrations have shown that hot-electron photodetectors can operate at terahertz speeds [60]. These detectors have very low dark noise and can operate at a very broad spectral range with applications [60].

3. CMOS Dominance on Image Sensors

3.1. CCD Imagers

The charge-coupled device (CCD) imager was invented by Willard Boyle and George Smith in 1969 [61–63] and was the reason why they were awarded with the Nobel Prize for Physics in 2009 [64]. Since then, it has become one of the most prolific imaging sensors with use in a wide range of applications. The CCD imager is a semiconductor sensor made of silicon and roughly composed of a matrix of coupled capacitors. Figure 7a shows a cross-section of a conceptual CCD array, where two regions can be identified in the substrate, e.g., the photo-active region and the transmission region [61]. The MOS capacitors act as photodetectors and are located above the photo-active region, while a shift-register controls the charge flow in the transmission region. The MOS capacitors receive a positive voltage bias directed to the gate electrode. This voltage causes holes to be pushed away from the region underneath the electrode, thereby forming a depletion region. A pair of electric charges is generated when a photon impinges the depletion region of silicon, with the electron being stored on the capacitor on top.

As shown in Figure 7b–f, during the reading, each capacitor is able to transfer its electrical charge to a neighbor capacitor, under the control of an external circuit [61]. Figure 8a illustrates the concept of a readout circuit used in CCD, which is composed of several columns with an array of capacitors [65]. The columns are multiplexed according to a selected scheme, e.g., a sequence of complete columns or interleaved data from the columns. The stored charge in the different capacitors (e.g., the transduction data) across the array is transferred sequentially between adjacent capacitors into the output of the array towards the last capacitor. A charge-to-voltage conversion is carried out in the last capacitor to allow its conversion into the digital domain. In conclusion, since the data are

transferred serially out of the array, it is not possible to read a random capacitor in the array other than the one in the last position [65].

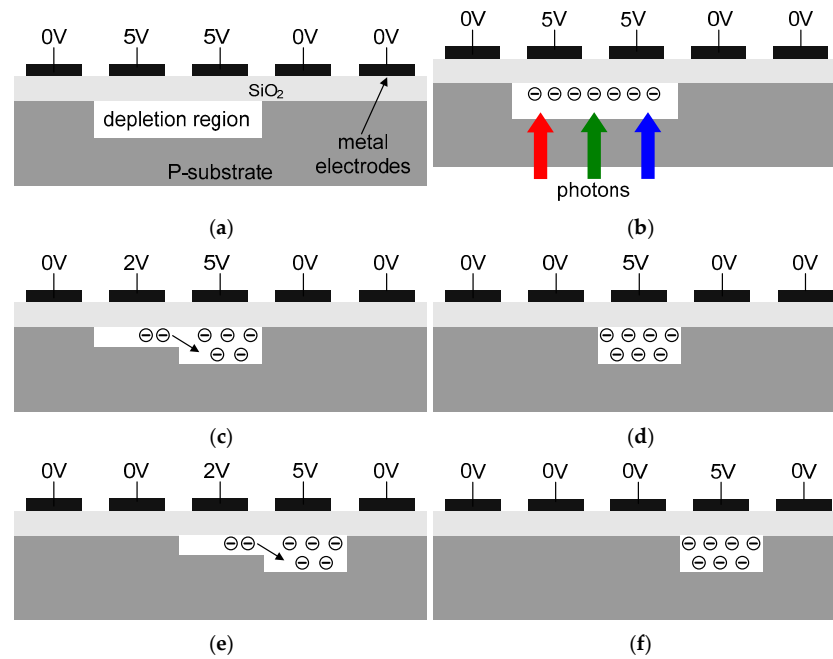


Figure 7. (a) Cross-section of a conceptual CCD array, and (b–f) a series of steps illustrating the programmable charge shift during the readout process.

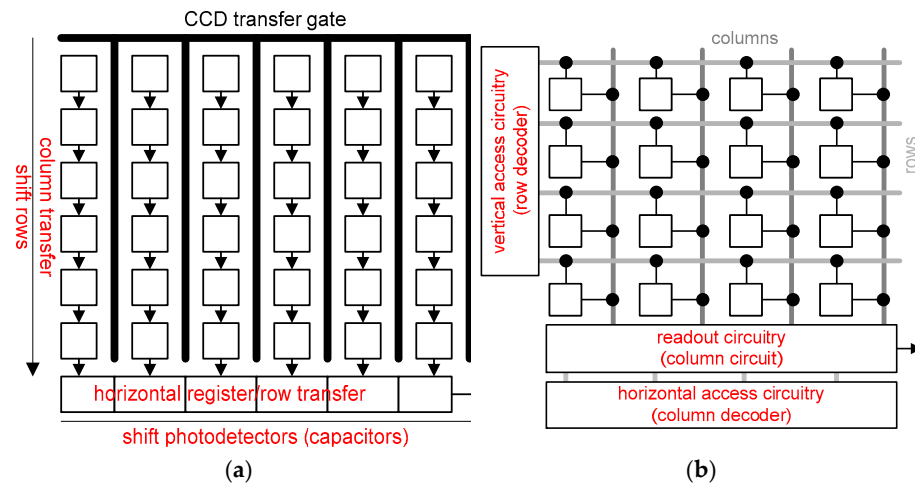


Figure 8. Concepts of readout circuit in (a) CCD and (b) CMOS. Adapted from Faramarzpour et al. [65].

The CCD itself is only composed of the capacitor array for the photon-to-electron conversion and charge transfer. Moreover, the CCD is implemented on a technology not coexistent with the technologies employed by the readout electronics, which can be CMOS or bipolar, among others [66]. This means that there is no possibility to integrate the CCD and the readout electronics into the same microdevice. A printed circuit board (PCB) is required to join these components. Figure 9 illustrates a block diagram of a conceptual CCD and the respective readout electronics, where this disadvantage is depicted [66].

Moreover, the CCD is prone to suffering from blooming and smearing [67]. Despite these disadvantages of a CCD over the CMOS, the former presents a comparatively larger dynamic range and high quantum efficiency from the visible region to the vacuum UV region, low dark current, low noise, linear response, and negligible geometrical distortion [68–70]. The fill factor is the ratio of the photo-sensitive area to the total area and it is 100% in the case of

a CCD [70]. For these reasons, CCDs are extensively used due to their low-light image ability and have not become obsolete despite the market dominance of CMOS.

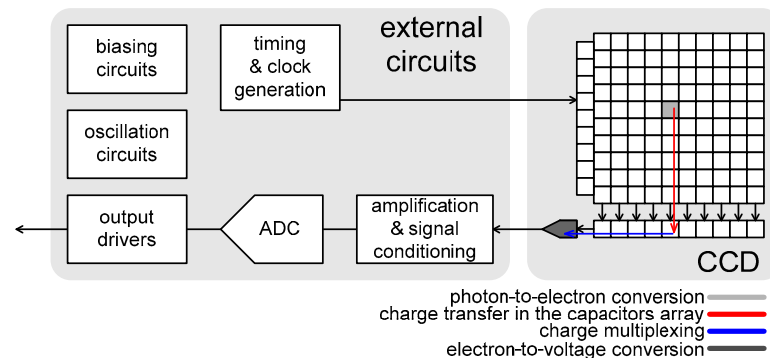


Figure 9. Block diagram of a CCD with readout electronics. Adapted from Litwiller [66].

3.2. CMOS Imagers

Due to the inherent advantages of CMOS technology, these imagers are present everywhere, such as in cellphones, cameras, security systems, traffic devices, medical equipment, and indoor positioning systems, among many others [71–73]. Figure 8b illustrates the concept of the readout circuits used in a CMOS, which is also composed of several columns with arrays of photodetectors [66,73]. This figure illustrates a generic CMOS imager architecture, which normally comprises a row decoder to select the row of pixels, a column decoder to select the column selecting, and thus, the pixel to read [74]. This architecture is very similar to random access memory (RAM) architecture in terms of its simplicity. Contrary to what happens in a CCD, these photodetectors can be accessed and read randomly. In a CMOS, the charge-to-voltage conversion is achieved at the photodetector level, followed by a multiplexer. As illustrated in Figure 10, one killing advantage of a CMOS over a CCD is the possibility to integrate the imager with other electronic circuits in the same microdevice [66].

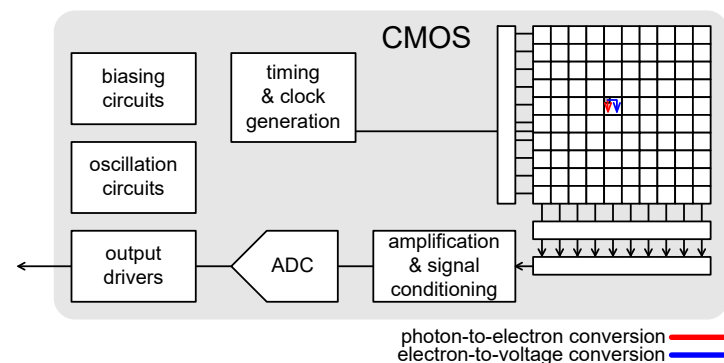


Figure 10. Block diagram of a CMOS imager with readout electronics, both integrated in the same microdevice/substrate. Adapted from Litwiller [66].

CMOS offer several advantages over CCD technology such as reduced power consumption, cost-effectiveness, increased integration capacity, on-chip functionality, selective data reading allowing random access to the image data, a single master clock, faster imaging speeds, and the ability to prevent blooming and smearing [68,69]. Furthermore, CMOS imagers are progressively shrinking in size, yet they continue to deliver high-resolution images packed with a dense array of photodetectors [74]. However, the dark current level of CMOS imagers is [still] an order of magnitude higher larger than that reported for CCDs [75]. Despite CMOS imagers presenting lower power consumption, this key issue is often overlooked. A work dedicated to this issue and a solution for optimum power consumption was proposed by Freitas et al. [76].

4. Architectures

4.1. Photocurrent Integration

It is necessary to define the pixel concept before presenting the phenomenon of photocurrent integration. The pixel is the elementary cell on an array of photodetectors, with each one being composed of an individual photodetector in the array and [when applicable] the respective readout circuit. Figure 11 illustrates the three types of pixels, which are drawn as being connected one to the other in both the vertical and the horizontal directions, as if it were a construction made with LEGOs [65].

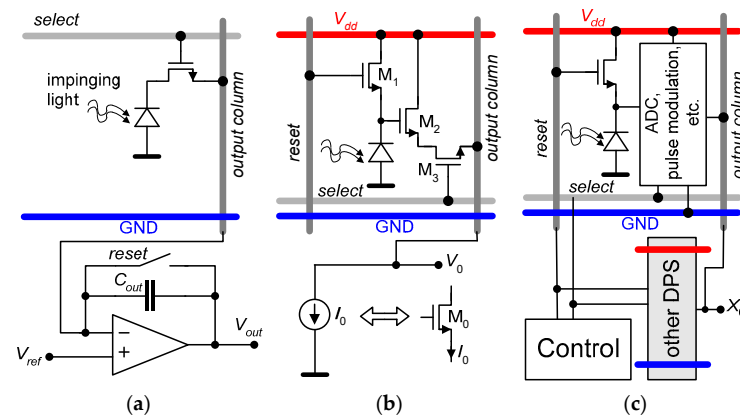


Figure 11. Types of pixels that work with charge accumulation: (a) a passive pixel sensor (PPS), (b) an active pixel sensor (APS), and (c) a digital pixel sensor (DPS).

The first type of pixel used on CMOS image sensors and presented in this paper is the passive pixel sensor (PPS) [65,77], whose structure is shown in Figure 11a. The PPS is simply composed of a photodetector and a transistor to select and connect the pixel to the readout circuit [65,77]. The selection of this photodetector in the pixel is achieved as follows: the NMOS is the pixel address transistor and works as a switch controlled by the *select* signal, connecting or disconnecting the photodetector to the output column. This column acts as a shared bus, which is selected for reading by the column circuit illustrated in Figure 8b. The photogenerated charge is transferred to the output column during the readout phase when the select signal puts the transistor switch into conduction. A column charge amplifier makes the charge-to-voltage conversion on each column. This charge amplifier is also referred to as a capacitive transimpedance amplifier (CTIA). The reading is destructive in the same way as happens with dynamic random-access memories (DRAMs). Ideally, the output voltage will be:

$$V_{out} = V_{ref} + \frac{Q}{C_{out}}, \quad (5)$$

for a transferred charge Q [C] on the photodiode. Finally, the output voltage V_{out} [V] can be converted into a binary word in the digital domain before the next reset to discharge the capacitance C_{out} [F] and to set the output of charge amplifier to V_{ref} [V]. It is possible to obtain very compact layouts of these pixels by extending the drain of the NMOS, performing the function of the N^+ / P -sub photodiode illustrated in Figure 6a. This pixel is the one that ensures the highest fill factors [78] of up to 80% [79], being limited only by the metals in the select and ground lines and output column lines blocking light transmission into the active area. This pixel also allows large voltage swing and simplicity of layout. The main drawback is that the pixel connects directly to the output column, adding the junction capacitance of photodiode to the long capacitance of the output column, resulting in long response times and excessive noise charge, degrading the signal-to-noise ratio [80]. The conversion of charge into voltage does not happen inside the pixel itself but takes place in the charge amplifier. Consequently, any disruptions along the column line significantly affect the charge signal, resulting in reduced sensitivity and increased noise [78,80].

Figure 11b illustrates the second type of pixel, i.e., the active pixel sensor (APS) [65,81–87], which consists of a matrix of pixels in the same way as the PPS, but with the difference of containing three MOSFETs, where M_1 is the reset transistor, M_2 is the amplifying transistor, and M_3 is the pixel address transistor. The APS has three modes of operation: the reset mode, the integration mode, and the readout mode [12,22,35,88–90]. The reset signal closes the reset transistor M_1 during the first mode and directly connects the N-type region of the photodetector to the supply voltage V_{dd} . In this mode, the transistor M_1 charges the capacitance junction of the photodiode, settling the potential of its cathode to the voltage supply V_{dd} [V]. The capacitance junction $C_{junction}$ [F] of the photodetector connected to the source and gate terminals of transistors M_1 and M_2 , respectively, is charged to $V_{g2} = (V_{dd} - V_{thn1})$, with V_{thn1} [V] being the threshold voltage of the transistor M_1 . During the integration mode, the photodiode is left floating. In this mode, the photodiode discharges at a rate proportional to the optical power P_i [W] impinging into the surface of the photodetector. The photogenerated current I_{ph} [A] modeled by Equation (1) is responsible for discharging $C_{junction}$ and decreasing the voltage V_{g2} by the amount ΔV [V] after an elapsed time of ΔT [s]. This voltage is then given by:

$$V_{g2} = (V_{dd} - V_{thn1}) - \Delta V_{in}, \quad (6)$$

with the voltage ΔV_{in} [V] being modeled by:

$$\Delta V_{in} = \left(\frac{I_{ph}(P_i)}{C_{junction}} \right) \times \Delta T \quad (7)$$

The resultant voltage V_{g2} [V] with information about P_i is then given by:

$$V_{g2}(\Delta t) = (V_{dd} - V_{thn1}) - \left(\frac{I_{ph}(P_i)}{C_{junction}} \right) \times \Delta T \quad (8)$$

This means that the rate of discharge increases with P_i , with V_{g2} decreasing. Thus, after a given amount of time ΔT , it can be readout and converted into the digital domain. The transistor M_3 acts as a simple switch, connecting the source of the transistor M_2 to the output column when the select signal is activated during the readout mode. The transistor M_2 works as a common drain amplifier (a unitary gain of the source follower was assumed for the sake of simplicity). The biasing voltage V_{bias2} [V] of the transistor M_2 is given by the mean value of $V_{g2}(t)$ calculated along a temporal sliding window with a length of $N \cdot \Delta T$ [s], where the mean number of reading cycles N must be at least 10 times to achieve a stable and quasi-constant biasing voltage V_{bias2} . The biasing voltage V_{bias2} of M_2 is given by:

$$V_{bias2} = \overline{V_{g2}(t)} = \frac{1}{N \cdot \Delta T} \int_0^{N \cdot \Delta T} V_{g2}(t) dt \quad (9)$$

Therefore, the voltage at the source of the transistor M_2 is:

$$V_{s2}(t) = (V_{s2,DC} - V_{bias2}) + V_{g2}(t) \quad (10)$$

with $V_{s2,DC}$ [V] being the DC voltage at the source of the transistor M_2 . The voltage at the output of the pixel is then given by:

$$\begin{aligned} V_{out}(t) &= V_{s2}(t) - V_{thn3} \\ &= (V_{s2,DC} - V_{thn3} - V_{bias2}) + V_{g2}(t) \end{aligned} \quad (11)$$

with V_{thn3} [V] being the threshold voltage of the transistor M_3 . The output signal of the APS is almost ready to be amplified, but not before subtracting the voltage $V_{out,DC}$ [V]. This process is known as correlated double sampling (CDS) [91–93] and measures the output signal twice. The first measure is performed in a known condition, while the

second reading is performed in an unknown condition. Afterward, the measured value obtained under known conditions is subtracted from the value acquired under unknown conditions. This subtraction yields a value that maintains a known correlation to the physical quantity being assessed, e.g., the optical power. The known condition is achieved for $V_{g2,1} = (V_{dd} - V_{thn1})$, resulting in $V_{out1} = (V_{s2,DC} - V_{thn3} - V_{bias2}) + (V_{dd} - V_{thn1})$, while the unknown condition is achieved for $V_{g2,2} = V_{g2}(\Delta T) = (V_{dd} - V_{thn1}) - [I_{ph}(P_i)/C_{junction}] \times \Delta T$, resulting in $V_{out1} = (V_{s2,DC} - V_{thn3} - V_{bias2}) + (V_{dd} - V_{thn1}) - [I_{ph}(P_i)/C_{junction}] \times \Delta T$. After the sampling and holding process of V_{g2} , the samples $V_{g2,1}$ and $V_{g2,2}$ are subtracted by a differential amplifier:

$$\Delta V_{out} = V_{g2,1} - V_{g2,2} = + \left(\frac{I_{ph}(P_i)}{C_{junction}} \right) \times \Delta T \tag{12}$$

or simply, $\Delta V_{out} = \Delta V_{in}$ [V]. The CDS process mixes and interleaves two sets of integration and readout modes because two samples $\{V_{g2,1}, V_{g2,2}\}$ of V_{g2} are required. All the pixels of a line share the same output column, originating so-called fixed-pattern noise (FPN), which impossible to reduce with filtering techniques [94–98].

Figure 11c depicts the general structure of a digital pixel sensor (DPS), where the data conversion from the analog to the digital domain is carried out at the pixel level by a dedicated ADC controlled by the reset and select signals [65,99–103]. The output of each pixel is a digital signal with all ADCs working in parallel. This results in a high-speed digital readout without FPN and it scales well with CMOS technology. However, DPS arrays have low fill factors because they contain more circuit blocks and more transistors per pixel [65]. Moreover, these pixels suffer from the quantization noise inherent to the ADC conversion, limiting applications where ultra-sensitive measurements are required. The integration process is present in the majority of pixels, as well as in the readout architectures and applications described in this paper.

4.2. Readout Architectures

It is essential to convert the photocurrent into another quantity enabling the analysis and the study of the obtained values after the selection of the pixel type. The main circuit options available are current-to-voltage (IV) and current-to-frequency (IF) converters.

4.2.1. Current-to-Voltage (IV) Converters

Figure 12a illustrates the schematic of a simple current-to-voltage (IV) converter. This circuit works as follows: the capacitor C [F] is fully charged at $V_{out} = V_{ref}$ [V] when the RESET is enabled (with RESET = “1”). The current I_{pd} [A] depends on the optical power P_i [W]; thus, $I_{pd} = I_{pd}(P_i)$. The current I_C [A] is mirrored by the PMOS transistor M_2 and given by $I_C = I_{pd}(P_i) \times (W/L)_2 / (W/L)_1$. The current I_C is effective only when RESET = “0”. The difference in the output voltage relative to V_{ref} [V] at the terminals of the capacitor ΔT seconds after the RESET signal changed from “1” to “0” and depends directly on the photogenerated current $I_{pd}(P_i)$, i.e., it depends on the optical power and is given by:

$$\Delta V_{out} = V_{out}(\Delta T) - V_{ref} = + \left(\frac{I_C}{C} \right) \times \Delta T = + \frac{I_{pd}(P_i)}{C} \times \left(\frac{W}{L} \right)_2 \times \Delta T \tag{13}$$

The output voltage V_{out} is equal to $V_{ref} + \Delta V_{out}(\Delta T)$ after ΔT seconds and can be converted to the digital domain. On the one hand, the integration time ΔT cannot be too low to avoid the risk of the output voltage being much lower than the maximum voltage convertible by the ADC, wasting the ADC’s useful conversion range. On the other hand, the integration time cannot be excessively high to prevent the integration from quickly reaching the maximum voltage convertible by the ADC. It is then clear that the reference voltage V_{ref} and the integration time ΔT must take into account in a compromise solution. Figure 12b depicts a

photograph of a microdevice fabricated in CMOS 0.7 μm from the on semiconductor [100]. This photograph also depicts the detail of an array of eight IV converters (green square on the left) and the detail of a matrix of 4×4 P⁺/N-well photodiodes (green square on the right). Each IV converter has an analog multiplexer (not shown in Figure 12a) with two inputs; each one connected to the cathode of a single photodiode. Each IV converter was designed and fabricated with $(W/L)_1 = 5 \mu\text{m}/3.5 \mu\text{m}$, $(W/L)_2 = 200 \mu\text{m}/0.7 \mu\text{m}$, and a capacitor C implemented with an NMOS transistor with $(W/L) = 44 \mu\text{m}/1 \mu\text{m}$ with its gate connected to the drain of M_2 and with their drain and source terminals connected to the ground.

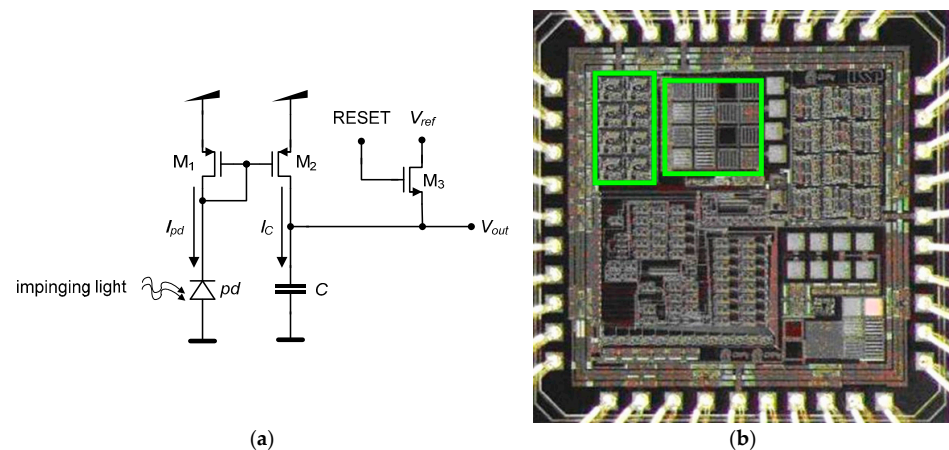


Figure 12. (a) Schematic of a simple current-to-voltage (IV) converter, and (b) an array of eight IV converters (green square on the left); each IV converter is able to read two photodiodes at a time and has its respective array of 4×4 photodiodes (green square on the right) [100].

It is essential to integrate a compact IV converter that offers high linear range, bandwidth, and a variable conversion gain with photodiodes. Figure 13 depicts the schematic of a simple IV converter as discussed by Ryszard Wojtyna [104]. The circuit is composed of two PMOS transistors forming a current mirror. Two other NMOS transistors, which are connected in series, create a nonlinear resistor. One of the NMOS operates in the triode region, enabling the achievement of a quasi-linear current-to-voltage conversion in a wide voltage range. The transistor size of the converter, namely the M_4 transistor, has an important role in the IV converter's behavior. The length of the M_4 transistor channel must be higher than the width [104].

Another approach, discussed by Srinivasan et al. [105], uses the output impedance of transistors to perform the current conversion. The schematic of this approach is illustrated in Figure 14. The IV conversion is performed using transistors that form a common-source amplifier with an active load and two current mirrors. Furthermore, it defines a reference voltage for no signal input through the use of an operational amplifier. It is important to highlight that the conversion gain is determined by the output impedances of the transistors and can be intentionally designed to be significantly high [105]. The variation of the voltage at the output of this circuit is given by [105]:

$$\Delta V_{out} = (R_{o1} || R_{o2}) \times \Delta I_{in} \quad (14)$$

where r_{o1} [Ω] and r_{o2} [Ω] are the impedances seen from the drains of transistors M_1 and M_2 , respectively. The current produced by the photodetector I_{in} [A] is mirrored by the two current mirrors, causing the current $I_{bias} + I_{in}$ to flow through M_2 . The current through M_1 is set to I_{bias} [A]. Finally, the difference in current ΔI_{in} [A] causes a change in the output voltage.

As a possible application of this type of readout converter, Chodavarapu et al. developed a CMOS vertical-type phototransistor array integrated with a IV converter, using the AMI 1.5 μm CMOS process through MOSIS, applied in a luminescence oxygen multi-sensor

system [106]. As depicted in Figure 15, the detector system is composed of a vertical-type photodetector array, a current mirror, and a current-to-voltage converter. The current mirror is formed through M_1 - M_5 transistors and causes a current gain of 10. The amplified current I_{total} [A] causes variation in the drain current through M_6 . The current through M_6 is mirrored to M_7 , and, as V_{bias} [V] is fixed, the output voltage V_{out} [V] varies for different values of I_{total} .

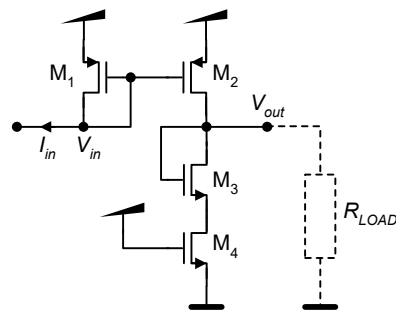


Figure 13. Schematic of a simple IV converter. Adapted from Ryszard Wojtyna [104].

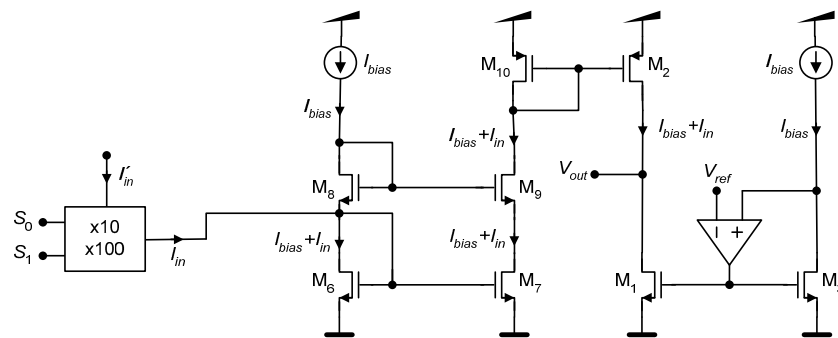


Figure 14. Schematic of the current-to-voltage converter proposed by Venkatesh Srinivasan et al. [105].

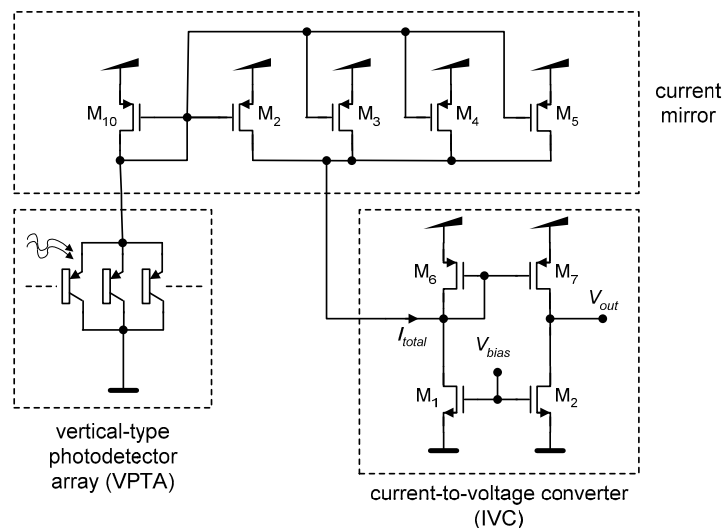


Figure 15. Schematic of a current-to-voltage converter integrated with a CMOS vertical-type phototransistor array, as proposed by Chodavarapu et al. [106].

4.2.2. Current-to-Frequency (IF) Converters

Regarding current-to-frequency (IF) converters, most of them use a capacitor that is charged or discharged by the current produced by the photodiode. The charge and discharge of the capacitor is controlled by a trigger circuit. The trigger circuit is the main difference between IF converters reported in the literature. The discharge pulse can be controlled through the implementation of comparators [107,108], Schmitt triggers [29,109,110]

or even with the use of RS flip-flops [111]. More specifically, IF converters based on comparators are not immune to noise, mainly for low currents. However, Kuo et al. developed a system of averages, comparing 100 results, to reduce the effect of noise [108]. Unlike comparators, trigger circuits based on Schmitt triggers, due to their greater noise immunity, good linearity, and reliability, are not subjected to extra calibration circuits and, therefore, allow for greater size reduction [29]. Ferreira et al. designed an IF converter based on a Schmitt trigger circuit in 0.18 μm technology, with a maximum frequency of 135 MHz, a maximum current of 80 μA , a linear behavior above 1800 nA, and a power consumption of 0.94 mW [110]. A schematic circuit based on a Schmitt trigger circuit is presented in Figure 16. This circuit is based on a PMOS transistor M_1 that operates as a capacitor. The PMOS transistor M_2 is responsible for discharging the capacitor M_1 , like a discharge transistor. Furthermore, an on/off system turns the circuit on and off, while a D flip-flop ensures a duty cycle of 50% at the output. As Ferreira et al. [110] demonstrated, the photodetector current charges the capacitor by connecting the drain to the source of the PMOS M_1 . The charging process of the capacitor can be checked through the V_{cap} [V] signal, visible in Figure 16. The voltage at the terminal V_{cap} originates a low-logic-level pulse of approximately 1 ns at the $V_{Trigger}$ terminal when it reaches a value of 0.6 V [110]. During this pulse, the capacitor M_1 discharges due to the current passing through the PMOS transistor M_2 until it reaches 1.3 V in V_{cap} terminal. This capacitor charging and discharging cycle is repeated several times so that a square signal with a certain frequency is obtained at the output of the D flip-flop [110].

Figure 17a shows the block diagram of another IF converter [12,35]. The purpose of this circuit is to transform light into a pulsed signal, where the frequency escalates in a manner corresponding to the intensity of the light. It comprises the photodiode operating in accumulation mode, which undergoes periodic resetting facilitated by the digital electronics. The reset pulse is settled by the reference voltage V_{ref} [V]. The supply voltage V_{dd} [V] is applied in the photodetector at the beginning of the working process when the switch closes. The supply voltage V_{dd} [V] is applied to the photodetector to charge the junction capacitance. The voltage at the terminals of the photodetector is maintained at V_{dd} , while the switch remains closed. A very small reverse-photogenerated current establishes across the junction of the photodetector, after the opening of the switch, and discharges the accumulated charge. The intensity of the photocurrent increases with the intensity of the light. The photocurrent decreases V_{pd} [V]. The rate of decrease in V_{pd} increases if the intensity of the light also increases. Figure 17b illustrates two situations for two photocurrents I_{ph1} [A] and I_{ph2} [A], with $I_{ph2} > I_{ph1}$. The voltage V_{pd} will cross below V_{ref} . Two clock cycles after this crossing, the digital electronics will generate a new reset signal to the switch. This process will cyclically repeat by itself. As illustrated in Figure 17c, the pulse frequency increases if the voltage V_{ref} also increases. This information can be used as an IF conversion. Moreover, the voltage V_{ref} facilitates the adjustment of the optimal settings. The comparator must be activated by the edge of a system clock. Figure 17d presents the schematic circuit of a possible edge-triggered comparator.

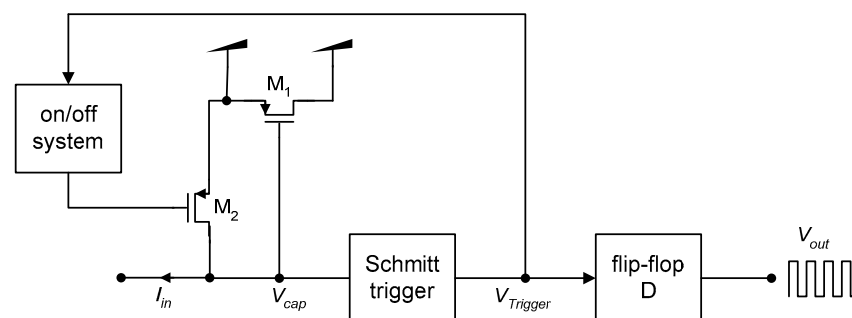


Figure 16. Schematic of a current-to-frequency converter based on a Schmitt trigger circuit [110].

5. Applications

Optical sensors in CMOS are being used extensively in the medical field as a key element in spectroscopy analysis. More specifically, they have been a great advance in the detection of gastrointestinal dysplasia and in the studies of Malaria infection. Furthermore, they have been applied in labs-on-a-chip and, more recently, in organs-on-a-chip devices and X-ray imaging. Optical sensors in CMOS are also promising solutions for other types of applications such as, for example, in photovoltaic (PV) sub-modules to measure the angles of incident light in the PV panels.

5.1. Detection of Gastrointestinal Dysplasia

As shown in Table 1, the optical detection of gastrointestinal (GI) dysplasia has been extensively studied and investigated. Most of the prototypes developed contain complex and bulky spectroscopy systems, with high-quantum-efficiency detectors (CCD or CMOS photodiodes [112,113] or optical multichannel analyzers [114]), but with large dimensions and difficult integration. To overcome the problems of macroscopic equipment and low integration levels, some authors have designed CMOS photodiodes to analyze GI tissues and to extract quantitative information [29,115,116]. As reported in [29], Correia et al. designed, fabricated, and characterized an integrated CMOS optical detection microsystem for the detection of GI dysplasia. The system is composed of two pn-junction photodiodes based on N⁺/P-sub and P⁺/N-well junctions using the N-well 0.7 μm CMOS process from the on semiconductor. In these fabricated photodiodes, the first and second oxides were retained due to fabrication limitations. To facilitate the readout process, the photodiodes were combined with light-to-frequency converters. These converters were tasked with generating a digital signal whose frequency aligns proportionally with the photodiode current. After microdevice fabrication, both photodiodes were characterized and presented a maximum quantum efficiency of 35% (at 470 nm) and 45% (at 640 nm) for the P⁺/N-well and N⁺/P-epilayer photodiodes, respectively. Furthermore, a dark current of 0.144 pA (1.44×10^{-17} A/μm²) and 4.390 pA (4.39×10^{-16} A/μm²) at 0 V was measured for the N⁺/P-sub and P⁺/N-well, respectively. The authors of this work used the same setup described in Section 2.1 and shown in Figure 4, i.e., they utilized a 250 W quartz tungsten halogen lamp as the light source. This light was directed through a monochromator and an optical fiber, guiding it into a contained microsystem. Current generated by the photodiodes was measured using a Keithley 487 picoammeter, powered by a voltage source. An oscilloscope (LeCroy 9310) was employed to assess the output frequency of the light-to-frequency converter. Additionally, a Hamamatsu S1336-5BQ commercial photodiode was utilized as a reference to measure the quantum efficiency of the fabricated photodiodes [29].

Table 1. Specifications of optical detectors for detection of gastrointestinal dysplasia.

Ref.	Manufacturer	Detector Type	Readout Electronic	Sensitivity	Dimensions	Application
[114]	nd	Optical Multichannel Analyser	nd	79%	nd	Optical techniques, such as fluorescence, reflectance, and light-scattering spectroscopies
[112]	S1226, Hamamatsu, Japan	Silicon photodiode	Low-noise current amplifier	nd	2.24 × 2.24 mm ²	Hybrid optical system to quantify the absorption and scattering coefficients of phantoms
[113]	S1227-66BR, Hamamatsu USA	Silicon photodiode	Current amplifier	nd	5.8 × 5.8 mm ²	Absorption and scattering coefficient quantification of tissue phantoms.
[29]	0.7 μm CMOS	N ⁺ /P-sub P ⁺ /N-well	IF converter	28 Hz/nA 280 Hz/nA	100 × 100 μm ²	Extraction of diffuse reflectance signals of the GI tissues
[115]	0.18 μm CMOS	N ⁺ /P-sub	IF converter	nd	822 × 936 μm ²	Spectroscopy analysis from diffuse reflectance light originated in the gastrointestinal tissue.

nd = non defined.

The researchers successfully demonstrated the utilization of CMOS optical sensors to capture diffuse reflectance signals using two-liquid homogeneous phantoms, with variable concentrations of an absorber and a scatterer, to replicate the absorption and scattering

properties of the GI tissues. This breakthrough paves the way for integrating these sensors into a biological microsystem for extracting spectroscopic signals, aiding in the early detection of gastrointestinal (GI) cancers. This integration eliminates the necessity for a costly optical microsystem for readout purposes. Additionally, also in [115], a CMOS-based microelectronics system is showcased for integrating photonic modules onto endoscopic capsules (ECs). The system's development involves the creation of optical sensors tailored for spectroscopic analysis within ECs, utilizing diffuse reflectance light originating from gastrointestinal tissue. The design of this system took place using the mixed-signal/RF 0.18 μm CMOS process from the TSMC (Taiwan Semiconductor Manufacturing Company, Hsinchu, Taiwan). This microdevice includes an array consisting of 16 photodiodes along with their corresponding readout electronics. Additionally, a collection of 16 optical filters is intended for further fabrication atop this setup. The ultimate goal is to integrate this microdevice into endoscopic capsules. The plan involves placing a set of 16 optical filters on top of the photodiodes. Furthermore, an LED emitting light with a wide spectrum will be used to illuminate the tissue of the gastrointestinal tract [115].

From Table 1, it is possible to conclude that the CMOS detectors presented the best characteristics regarding the size and dimensions of the optical detector, its cost, and its outputting equal or better performance than the techniques where the CMOS technology was not used.

5.2. Detection of Malaria Parasites

In addition to the detection of GI dysplasia, CMOS photodiodes for malaria detection have also been applied. Hemozoin (Hz), or malaria pigment, is a valuable target for optical malaria diagnosis. It forms within the parasites' digestive vacuoles during hemoglobin digestion, representing 95% of the red blood cells' dry weight. Unique to parasites, Hz serves as a natural diagnostic marker absent in healthy individuals. Its concentration increases with parasite development and higher parasitemia levels, offering potential as a marker for disease progression and treatment efficacy assessment through quantification.

Taking advantages of the optical properties of hemozoin and based on a spectrophotometric microsystem for a medical field application, Ferreira et al. developed a CMOS-based microelectronic detection system designed to automatically assess the quantity of malaria parasites within a blood sample [110]. The system's architecture includes a set of 16 N^+/P -sub silicon junction photodiodes and 16 current-to-frequency (IF) converters. This microsystem was meticulously designed and manufactured using the CMOS process available from the UMC (United Microelectronics Corporation), specifically the L180 MM/RF technology. The authors chose this technology due to its integration on the same chip as high-frequency circuits, including acoustic sensors. The photodiodes, with an active area of $100 \mu\text{m} \times 100 \mu\text{m}$, presented a maximum quantum efficiency of 25% at 570 nm. Furthermore, the IF converter presented good linearity ($R_2 = 99.9\%$) of the converted current [110]. The CMOS microsystem presented a sensitivity of $4.5 \text{ Hz/parasite } \mu\text{L}^{-1}$ and was able to distinguish between healthy RBCs, and infected RBCs with 12, 25, and 50 parasites/ μL . The authors used 16 different wavelengths ranging from 400 to 800 nm. Frequency results were obtained from the IF converters and used to calculate slopes between the wavelengths, aiming to establish a decision algorithm based on the data. As parasitemia increased, the slopes connecting different wavelengths varied. The calculated slopes between the 16 output frequencies further distinguished healthy RBCs from different parasitemia levels. These results obtained by Gabriel et al. hold promise for the development of automatic detection and quantification algorithms, leveraging discrete data. To perform the experimental tests once again, the authors used an optical setup, composed of a light source of 250 W, a monochromator, an optical fiber, a black blanket to block the outside light, and a picoammeter. Furthermore, the cultured *Plasmodium falciparum* parasite samples were implanted in a 1 mm optical path cuvette. The cuvette was positioned to ensure that the light emitted through the fiber passes through the sample and reaches the CMOS photodetector [110]. This research documented the effective creation of intricately combined optical

CMOS sensors dedicated to malaria diagnosis. The outcomes demonstrated competitive results akin to gold standard diagnosis methods that only detect 50 parasites/ μL , marking a significant advancement in malaria research [110].

Pirnstill et al. devised a specialized design for a polarized microscope platform that utilizes a cell phone. This setup was engineered to detect birefringence specifically in histological specimens afflicted with the malaria parasite [117]. The phone employs an 8-Megapixel iSight camera with a CMOS back-illuminated sensor. The camera has a physical sensor size of 8.47 mm, with pixel dimensions of 3264×2448 , composed of $1.5 \mu\text{m}$ pixels [117]. The device is simple, compact, low-cost, durable, and presents a design capable of being used on multiple mobile device platforms. The authors demonstrated these capabilities using an iPhone 5s, obtaining a system with a resolution of $1.05 \mu\text{m}$, $50\times$ magnification, and a field-of-view (FOV) of $0.78 \text{ mm} \times 0.79 \text{ mm}$. The system successfully identifies hemozoin crystals, presenting comparable results to a reference Leica DMLM polarized microscope. The study emphasizes the importance of resolution and FOV in accurate parasitemia measurements and automated malaria detection. Future research aims to use human malaria strains, improve device compactness, durability, and usability, and reduce costs for field testing in Rwanda. The envisioned final product is expected to cost less than 1 USD per test result, and the design can be adapted to various commercially available phones. The current mobile-optical-polarization imaging device prototype costs around 7 USD, excluding the mobile phone.

Compared to other types of optical sensors and other malaria detection techniques for the detection and quantification of hemozoin [118–120], from Table 2 it is possible to conclude that the CMOS optical sensors designed and fabricated by Ferreira et al. enabled the diagnosis and quantification of malaria with a good detection limit and greater integration than the other methods, due the small size of the detectors. There are still not many works on the detection of malaria with CMOS photodiodes. However, this will be a possibility to consider, taking advantage of the optical properties of hemozoin.

Table 2. Specifications of detectors for malaria detection.

Ref.	Detector Type	Readout Electronic	LOD	Time	Detector Dimensions
[118]	PIN photodiodes	Transimpedance amplifier	$1 \mu\text{g}/\text{mL}$	Around 1 min	$2.73 \times 2.73 \text{ mm}^2$
[119]	Method of magnetic field-augmented SERS detection	nd	10 parasites/ μL	20–30 s	$7.0 \times 1.5 \text{ mm}^2$
[120]	Photodetector and a magnet	nd	26 parasites/ μL	nd	9.5 mm of diameter
[121]	Magnetic micro-concentrators	Lock-in Amplifier	40 tRBCs/ μL	nd	$1 \times 3.8 \text{ mm}^2$
[122]	Spectrophotometer	nd	10 Infected RBCs/ μL	$37 \pm 5 \text{ min}$	nd
[123]	UV-visible spectrophotometer	nd	$1 \mu\text{g}/\text{mL}$	$3 \pm 0.5 \text{ min}$	nd
[117]	CMOS back-illuminated sensor	Set Scale command in ImageJ	Less than 30 parasites/ μL	nd	$4.89 \times 3.67 \text{ mm}^2$
[110]	N ⁺ /P-sub CMOS	IF Converter	12 parasites/ μL	nd	$400 \times 400 \mu\text{m}^2$

nd = non defined.

5.3. X-ray Imaging

X-ray silicon microdetectors combined with digital data storage capacity find applications in medical imaging applications [124]. In traditional radiography, an X-ray source emits radiation that transmits through the body under study. This radiation reaches a photographic film, where it prints the pattern of the structures inside the body. This film is later developed revealing the image [125]. This form of obtaining images requires transporting the silver films for further processing in a specialized laboratory. These procedures, combined with handling and transporting logistics, often result in delays and, in the worst cases, in the confusion of test results with those of other patients.

Approaches based on arrays of microdetectors in silicon allow immediate visualization of the image without the necessity of silver films and photographic processing. Moreover, they enable the storage of images directly in digital formats [126]. CMOS technology has the

potential to capture X-ray images with lower radiation doses, and to produce high-quality images in real-time. This potential reduction in radiation exposure is particularly advantageous for patients, minimizing potential health risks associated with high radiation levels, especially in prolonged treatments. This lowers the cost of the device when compared with film-based X-rays [127]. The advantages associated with the digital format include the possibility of interactively adjusting the contrast and the brightness of the image while the exam is being conducted by a health professional. In conclusion, the digital format enables the use of digital signal processing (DSP) tools and machine learning algorithms to process and analyze the obtained images in real-time with much more accuracy.

N^+ /P-sub photodiodes are the preferable structures for imaging applications in general, and in X-ray imaging in particular, due to their inherently high quantum efficiency and responsivity in the visible portion of the electromagnetic spectrum [128]. Figure 18 illustrates the structure of N^+ /P-sub photodiodes (it is not to scale and it is the same structure illustrated on the right of Figure 6a). The X-ray absorption coefficient of silicon is low, with ≈ 277 electron-hole pairs being created for each 1 keV of absorbed X-ray photons [128]. One way to overcome this limitation is to use scintillator materials to convert X-ray radiation into visible light so as to generate a significant number of electron-hole pairs in the silicon photodetectors [128–133].

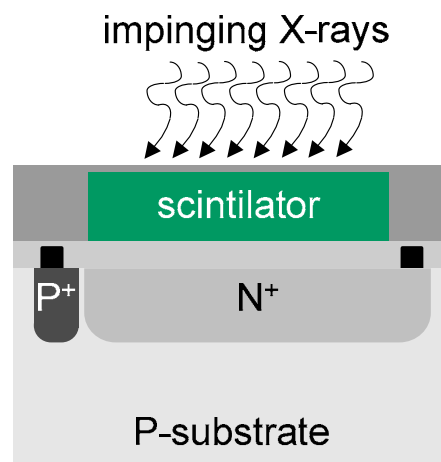


Figure 18. Concept of an X-ray detector based on a N^+ /P substate photodiode with a scintillation crystal and aluminum coating.

Thallium-doped cesium iodide (CsI(Tl)) is one of the most used materials for scintillating crystals in X-ray imaging [128–132]. The light yielded by CsI(Tl) presents a scintillation peak at 550 nm (e.g., in the green portion of the spectrum), with a decay constant of 1 μ s, and with a spectral range emission between 350 and 725 nm [128–132].

Silicon photodetectors can be combined with a variety of other scintillation crystals to produce light of different colors for specific applications [128,133]. For example, NaI(Tl), $Y_3Al_5O_{12}$ (Ce), CaI_2 , CsI:Na, ZnS(Ag), and CaI_2 can be used to yield light at the spectral peaks of 303 nm, 390 nm, 410 nm, 420 nm, 450 nm, respectively [133].

As also illustrated in Figure 18, the layer made of scintillating crystal converts the X-ray radiation into visible light [134]. Scintillating crystals are then used to produce light photons proportional to the amount of X-ray energy absorbed. The yielded light can now be converted into a photocurrent by the photodetector. The aluminum coating is required to prevent the loss of the back-emitted visible light and to prevent crosstalk between individual photodetectors [128,135]. Figure 19 illustrates the final results of several fabrication steps performed by Rocha et al. to present a CMOS X-ray detector proof-of-concept [128].

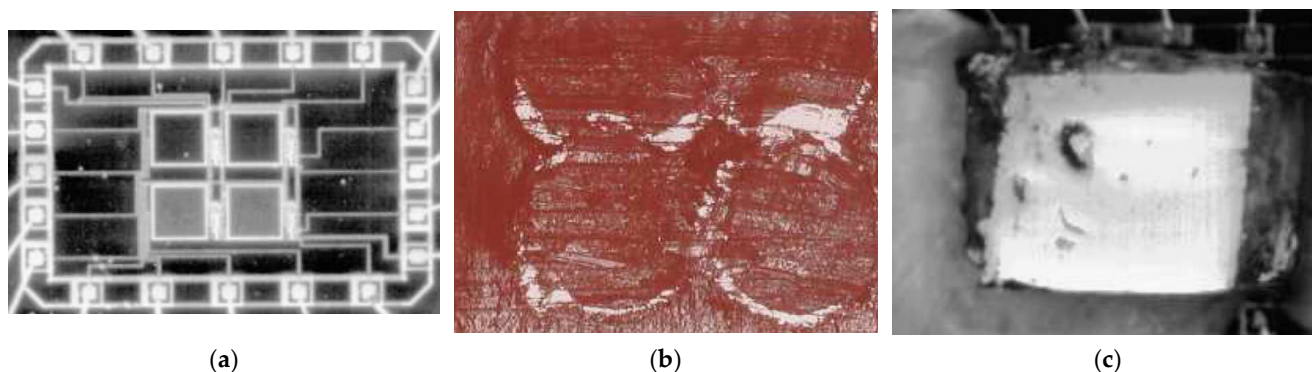


Figure 19. For a selected application of an X-ray sensor with an array of 2×2 pixels [128]: photographs (a) of a CMOS microdevice with an array of 2×2 pixels made of N^+/P sub photodiodes before positioning the array of CsI(Tl) scintillators, (b) of the CsI(Tl) scintillators placed inside the aluminum cavities, and (c) of the final prototype of the X-ray sensor. These figures were reproduced with previous authorization via Elsevier.

The photograph in Figure 19a shows a CMOS microdevice with an array of 2×2 pixels made of N^+/P -sub photodiodes before positioning the array of CsI(Tl) scintillators [128]. The photograph in Figure 19b shows CsI(Tl) scintillating crystals filling the aluminum cavities [128]. After that, the cavities were covered with a thin film of aluminum with a thickness of $10 \mu\text{m}$. Finally, the photograph in Figure 19c shows the final prototype of the X-ray sensor after the cavities covered with the thin film of aluminum were flipped and placed on top of the photodiodes [128]. The transmissivity of the aluminum with a thickness of $10 \mu\text{m}$ is relatively low for visible light.

The application of X-ray CMOS detectors is a well-known method and it is being used by several major brands as a cutting-edge technology. Table 3 lists the main characteristics of state-of-the-art research works.

Table 3. Main key characteristics of selected state-of-the-art works.

Ref.	Commercial Brand	Resolution	Size [cm^2]	Image Depth	Scintillator Material	Tube Voltage
[136]	Lassena (CsI)	2786×2400	24×14.1	14 bit	CsI:Tl	50–90 kV
[137]	GPixel	2048×2048	22.5×22.5	nd	CsI:Tl	40–2000 eV
[138]	Elekta	1024×1280	41×41	16 bits	nd	nd
[139]	Dexela 2923	1944×1536	11.5×14.5	nd	CsI:Tl	28–70 kV
[140]	Sharp-AMFPI	320×320	24×30	nd	CsI:Tl	30 kV

nd = non defined.

Alzahrani et al. [136] presents a new detector branded Lassena (CsI). This detector comprises an array of 3-T APS similar to the one illustrated in Figure 11b and it uses a coupled CsI(Tl) scintillator with a thickness of $1000 \mu\text{m}$. This CMOS sensor is also composed of a matrix of 2786×2400 pixels in an area of $24 \text{ cm} \times 14 \text{ cm}$, and a pitch of $50 \mu\text{m}$. The quantum efficiency is about 50% at 540 nm. The readout electronics contain an ADC with a resolution of 14 bits. This CMOS sensor was characterized by three X-ray beams, e.g., RQA3 with 50 kV, RQA5 with 70 kV and RQA7 with 90 kV. The detector presented linear responses with $R = 99.9\%$ for these exposures: 0.26 to $2.17 \mu\text{Gy}$ for RQA3 and 0.29 to $1 \mu\text{Gy}$ for RQA5 and RQA7.

Desjardins et al. [137] used a camera equipped with a commercialized backside-illuminated scientific CMOS (sCMOS-BSI) sensor with an array of 2048×2048 pixels, a pixel size of $11 \times 11 \mu\text{m}$ per pixel, and a physical size of $22.5 \text{ mm} \times 22.5 \text{ mm}$, creating a four-megapixel sensor, with a pixel pitch of $21 \mu\text{m}$. They used a soft X-ray beam with

an energy between 30 and 2000 eV to characterize the CMOS sensor, where a quantum efficiency higher than 90% in the lower energy range was observed.

Son et al. [138] evaluated image quality in radiation therapy using an Elekta iviewGT, a 1024×1280 pixel sensor with a size of $41 \text{ cm} \times 41 \text{ cm}$, and a pixel pitch of $172 \mu\text{m}$ with an image depth of 16 bits. They evaluate the MTF (modulation transfer function), NPS (noise power spectrum), and DQE (detective quantum efficiency), which showed high accuracy in radiation delivery at the spatial frequency in 1.0 mm^{-1} .

Konstantinidis et al. [139] used the Dexela 2923 CMOS sensor to acquire X-ray images. The CMOS X-ray sensor comprises an array of 1944×1536 pixels with a pixel pitch of $75 \mu\text{m}$ in a package size of $11.5 \text{ cm} \times 14.5 \text{ cm}$. The performance of the CMOS sensor was evaluated with a Varian RAD-70 with the voltage settled between 28 kV and 70 kV.

Scheuermann et al. [140] used a Sharp-AMFPI that is composed of an array of 320×320 thin-film transistors (TFTs) with an active area of $24 \text{ cm} \times 30 \text{ cm}$ with a pixel pitch of $85 \mu\text{m}$. The optical performance of their X-ray sensor was characterized with a 30 kVp Mo/Mo beam. The Sharp-AMFPI X-ray sensor was able to achieve an optical avalanche gain of 76 ± 5 at an electric field E_{Se} up to $105 \text{ V} \cdot \mu\text{m}^{-1}$, being only limited by the optical spread of the CsI scintillator.

5.4. Labs-On-a-Chips (LOCs)

Optical CMOS sensors have also been increasingly studied in the area of clinical and biological analysis, due to their high integration rate, low cost, and portability, guaranteeing that the examination can occur at any site, delivering immediate findings [90,141]. Minas et al. developed an on-chip integrated CMOS optical detection microsystem for spectrophotometric analysis in biological microfluidic systems, through a double-metal, single-polysilicon $1.6 \mu\text{m}$ N-well CMOS process [90]. The microsystem is composed of N^+/P -sub photodetectors with an active area of $100 \mu\text{m} \times 100 \mu\text{m}$ and a light-to-frequency converter that integrated a comparator for readout. The photodetector presented a responsivity of 224 mA/W at $\lambda = 495 \text{ nm}$ and 223 mA/W at $\lambda = 592 \text{ nm}$. This specific wavelength marks the point where the uric acid molecule and total protein exhibit their highest absorption. The mentioned microsystem was created to seamlessly integrate into a biological setup for quantifying biomolecule concentrations in bodily fluids. Its functionality was demonstrated through the accurate measurement of uric acid levels and total protein in urine. The optical system's sensitivity was 1 kHz/Wm^2 at $\lambda = 670 \text{ nm}$. The final lab-on-a-chip created by Minas et al. presented a minimum detection capability of $0.5 \text{ mg} \cdot \text{dL}^{-1}$, with an achieved sensitivity of $5 \text{ mg} \cdot \text{dL}^{-1}$ for uric acid and total protein. This sensitivity corresponds to a relative resolution of 3.3%, meeting the requirements for human urine values. Additionally, the lab-on-a-chip successfully measured concentrations of uric acid and total protein while being illuminated by a 200 W halogen lamp source. CMOS integration enabled Minas et al. to develop a device possessing the equivalent reliability and precision of the spectrophotometric automated equipment utilized in state-of-the-art clinical analysis laboratories. Simultaneously, it is portable, cost-effective, provides comfort for the patient, and additional molecules or biological fluids could be considered as potential candidates for the lab-on-a-chip.

Furthermore, also in [142,143], CMOS photodiodes based on a $0.35 \mu\text{m}$ process were used. Both present a small size. However, one was applied for the detection of *Staphylococcus aureus* [142] and the other for several applications like diagnosing drug discovery [143]. In their study, Norian et al. [142] pioneered the use of CMOS technology to integrate all essential functions for quantitative polymerase chain reaction (qPCR) on a lab-on-a-chip platform. These include temperature control, heating, microfluidics, and fluorescence detection. For fluorescence detection, crucial for monitoring PCR progression, Haig et al. employed integrated single-photon avalanche diodes (SPADs) featuring a shallow P^+ region with a diameter of $7.5 \mu\text{m}$ within an N-well with a $15 \mu\text{m}$ diameter. Their work showcases how lab-on-a-chip devices can effectively utilize the advanced design capabilities of sil-

icon CMOS foundries. The authors achieved robust identification and quantification of *Staphylococcus aureus* using the proposed lab-on-a-chip [142].

Manaresi et al. [143] developed an optical sensing system using standard CMOS technology to detect single particles or clusters, allowing the manipulation of over 10,000 cells simultaneously. The authors detected the particles' presence using CMOS photodiodes with a $2\ \mu\text{m} \times 17\ \mu\text{m}$ well-junction photodiode placed underneath the $1.2\ \mu\text{m}$ wide gap, implemented with a CMOS APS. The device was optimized for handling eukaryotic cells (such as the lymphocytes found in blood) in the range of 20–30 μm . Manaresi et al. believe that the CMOS device developed has the potential to be an enabling technology for the creation of innovative protocols in cell biology. Its features include the ability to perform multiple experiments on individual cells simultaneously, detect and isolate rare cells in small samples, deliver compounds in a controlled manner to target cells, and investigate real-time cellular responses to chemicals and cell–cell interactions [143].

CMOS photodiodes have also been applied for other applications, such as *Giardia lamblia* imaging [144] and oxygen sensors [145], incorporating both into a lab-on-a-chip device. In [144], Lee et al. demonstrated the use of an OFM device to perform microscopy imaging of cysts and trophozoites of *Giardia lamblia*, using a CMOS optical sensor containing a 2D array of 1280×1024 square pixels. This enabled the authors to create an autonomous, inexpensive, and highly compact system for water quality analysis and monitoring in resource-limited areas.

In [145], Shen et al. employed a CMOS image sensor in a portable optical oxygen sensor. The sensor featured an active array size of 3488×2616 pixels, each approximately $1.75\ \mu\text{m} \times 1.75\ \mu\text{m}$, integrated with an ADC and a gain amplifier. The authors used PtOEP as the oxygen-sensing material. The emission intensities of PtOEP vary for different oxygen concentrations, consequently they alter the current measured by the CMOS sensor. The authors achieved high sensitivity and linearity in the Stern-Volmer analysis, calculated by:

$$\left(\frac{I_0}{I}\right) = 1 + K_{SV}[\text{O}_2] \quad (15)$$

where I_0 and I are the emission intensities in the absence and presence of oxygen at concentrations of $[\text{O}_2]$, respectively, and K_{SV} is the Stern–Volmer constant. The device demonstrated a sensitivity of the oxygen sensor, represented by the ratio I_0/I_{100} , of ≈ 41 . This result is comparable to the values of approximately 50 reported by others using an external spectrophotometer. The authors successfully demonstrated the device's utility, achieving sensitivity comparable to macroscale benchtop sensor systems, all thanks to the utilization of a low-cost CMOS sensor.

Hu et al. developed a CMOS microdevice comprising an array of 16×16 photodiode pixels. Each pixel incorporates a PN-junction with a traditional 3-transistor read-out design. The microdevice was manufactured utilizing a commercially accessible CMOS 350 nm four-metal process offered by Austria Micro Systems (AMS) [146]. The photodiode presented an output of $408 \pm 22\ \text{mV}$ in dark conditions, had a minimum detection of $50\ \text{nW}/\text{cm}^2$, and started to saturate when exposed to $4.9\ \mu\text{W}/\text{cm}^2$ [146]. The researchers integrated the PN-junction photodiode into a paper strip containing three microfluidic channels. They proved the simultaneous detection of potential sepsis biomarkers, glucose, and lactate [146]. The detection was carried out using absorbance measurements. It used an LED as a light source, located at the top, and the photodiode was located at the bottom of the paper strip. The authors showed that the voltage across the photodiode varies over time for different concentrations of glucose and lactate. Higher concentrations of analytes lead to lower photodiode voltages. They achieved a limit of detection (LOD) of approximately $520\ \mu\text{M}$ for glucose and $110\ \mu\text{M}$ for lactate, determined from three times the standard deviation of the blank signal. While previous biosensors have achieved lower detection limits, this one provides a sufficiently low LOD for the studied metabolites. By combining a cost-effective paper strip with microfluidic channels and a sensitive CMOS photodiode sensor array, they developed a sturdy, portable, and highly affordable biosensor device suitable for diverse

diagnostic tests across numerous applications, easily increasing the number of microfluidic channels [146].

Regarding the other options for labs-on-a-chip, most of them, as presented in Table 4, present more expensive [147], lower packaging density [28], and more complex systems [36]. The detector presented by Nieuwenhuis et al., presents a low-dimensions detector through a bipolar IC-process [148]. However, bipolar technology has a lower packaging density and higher cost than CMOS technology [28].

Table 4. Specifications of optical detectors integrated in labs-on-a-chip.

Ref.	Fabrication/Manufacturer	Detector Type	Readout Electronic	Characteristics	Detector Dimensions	Application
[90]	1.6 mm CMOS	N ⁺ /P-sub	Light-to-frequency converter	0.5 mg dL ⁻¹	200 × 200 μm ²	The quantitative measurement of uric acid and total protein in urine
[142]	0.35 μm CMOS	single-photon avalanche photodiodes (SPADs)	nd	nd	15 μm (diameter)	Detection of <i>Staphylococcus aureus</i>
[143]	0.35 μm CMOS	well-junction photodiode	Current-to-voltage converter	nd	2 × 17 μm ²	Diagnostics to drug discovery
[144]	Micron Tech, MT9M001C12STM	CMOS sensor chip	nd	nd	1280 × 1024 square pixels	<i>Giardia lamblia</i> imaging
[145]	Low-cost CMOS image sensor	nd	A/D converter and gain amplifier	nd	1.75 × 1.75 μm ²	Oxygen sensor
[146]	0.35 μm CMOS	nd	Classic 3-transistor read-out	LOD of 520 μM for glucose and 110 μM for lactate	CMOS chip (2 mm × 2 mm)	Glucose and lactate
[148]	Standard 1 μm bipolar IC-process.	Shallow photodiodes (0.25 μm)	Lock-in amplifier	nd	2.5 × 2.5 μm ² 50 × 1 μm ²	Microfluidic cytometer
[149]	AD500-8-TO52S2, Silicon sensor	low-cost avalanche photodiode	Current-to-voltage converter	0.2 nmol L ⁻¹	nd	Capillary and chip electrophoresis
[150]	PC5-6b T	PIN photodiode	Current-to-voltage converter	Resolution of 0.002 pH	nd	pH quantification
[151]	CR131, Hamamatsu, Japan	photomultiplier	nd	10 nM (superoxide); 5.6 nM (hydrogen peroxide)	nd	Simultaneously determining two or more reactive oxygen species (ROS) in a biological system.
[147]	IPX-11M5, Imperx, Boca Raton, FL	lensless CCD	nd	19.5 ng mL ⁻¹	nd	Detect ovarian cancer HE4 biomarker in urine at the point-of-care

nd = non defined.

5.5. Angular Measurements of Incident Light

Optical sensors in CMOS can find applications in solar trackers. It is widely known that solar radiation's angle of incidence is a key factor in determining the size and placement of photovoltaic systems. Solar trackers play a major role when designing the infrastructure and the power output of the panels. Normally, the angle is defined one single time using geographical positioning. However, this technique overlooks local elements like climatic conditions, terrain, and highly reflective buildings that can influence energy production. Costa et al. developed a photovoltaic (PV) sub-module with an optical sensor and readout electronics in a CMOS. The CMOS microdevice was designed to accurately measure the incidence angle of the solar light to automatically track the position of the photovoltaic cells [12]. The microdevice was fabricated using the 0.7 μm CMOS process from the on semiconductor. This microdevice is composed of an array of 4 × 4 N⁺/P-sub photodiodes and the respective readout circuits. As illustrated in Figure 20a, the photodiodes on a common line share the same current-to-frequency (IV) converter. Each photodiode converts light into pulsed signals. The digital signals SEL₀ and SEL₁ allow only one photodiode on a specific row to connect the IV converter of that row. The signals SEL₂ and SEL₃ select the input of the respective IV converter to connect to the multiplexer output. Figure 20a illustrates the block diagram of the complete solar tracker, while Figure 20b shows the photograph of the fabricated microdevice [12].

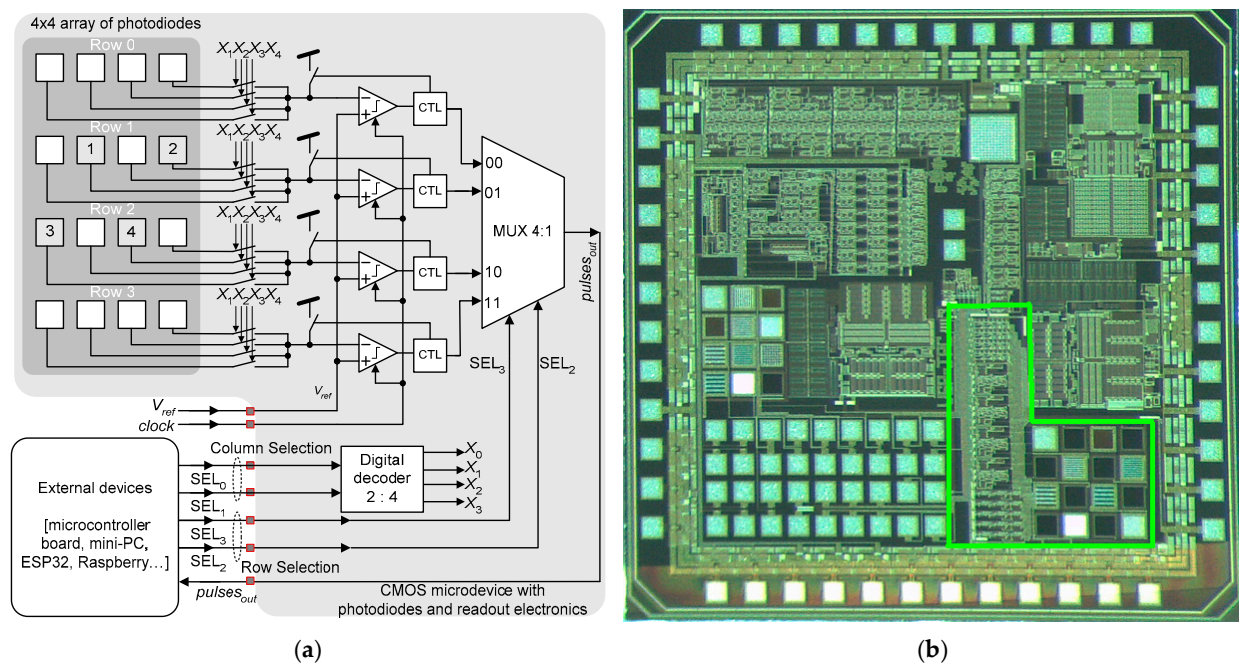


Figure 20. (a) Block diagram of the complete optical sensor developed by Costa et al. [12], (b) and the photograph of the fabricated microdevice with details of the solar tracker [152].

A set of metal microstructures with widths of 5 and 10 μm were created on top of the photodiodes to facilitate the measurements of the impinging light [12]. Each photodiode generates a response proportional to the angle of incidence. The transduction is based on producing a photocurrent with intensity matching the incoming light according to Equation (1) [12]. The selected IV converter generates a pulsed signal with a frequency that depends on the intensity of the light that reaches the surface of the respective photodiode.

A prototype of a PV sub-module with this CMOS microdevice was fabricated. The PV sub-module comprises an Arduino Uno board, an Arduino shield with a bus to connect a real time clock (RTC) module, a module with a micro-SD card to store the acquired data, and the CMOS microdevice with the optical sensor [12]. A box made of acrylonitrile butadiene styrene (ABS) was printed in 3D to enclose and protect the electronic circuits of the PV sub-module against harsh environmental conditions such as weather and dust. An optical attenuator was placed in the light aperture to prevent the saturation of the optical sensor. The PV-sub module measured 12 cm \times 10 cm \times 4 cm [12]. A series of initial tests were conducted in the laboratory to obtain the optimal parameters and frequency settings in order to avoid the saturation of the photodiode [12]. These tests preceded the final evaluation of solar incidence on the roof, where a setup was constructed to measure the angles and the corresponding frequencies of the pulsed signal. The laboratory setup featured a rotating arm with a bright LED at the top and a servomotor fixed at the arm's lower end. The laboratory setup was placed on top of an optical table to ensure mechanical stabilization against vibrations. The servomotor covered a range of rotation angles from 40° to 150° in steps of 5°, while the LED brightness was directly controlled by a potentiometer. The CMOS microdevice was supplied with a voltage supply of 5 V via the Arduino Uno. The reference voltage V_{ref} was settled to 2 V and obtained from the voltage supply via a potentiometer. The clock signal, CLK, was adjusted to 50 kHz using the CA4093 gated oscillator. The information about the instantaneous frequency of the signal *pulses_{out}* at the output of microdevice was acquired with the help of a frequency counter.

A second setup was used to track the solar position on the roof [12]. This configuration involved a servomotor tilting the case containing all of the sensor components, sweeping angles from -90° to $+90^\circ$. The PV sub-module's sensor was sensitive to both the east-west and north-south directions, necessitating an additional servomotor to sweep the

orthogonal direction. Unlike the laboratory setup, this system rotates the entire case, obtaining frequency measurements for all angles with approximate intervals of two minutes. The second setup was composed of the full PV sub-module, power supply source, and mechanical parts. This setup gave accurate information on the rotation angle without rotating the bulky PV panel. This setup is compact, occupying only 24 cm × 10 cm × 14 cm; thus, it is suitable for limited-space environments [12].

Costa et al. also developed another CMOS microdevice with an optical sensor and respective readout electronics [103]. This second microdevice is, in part, similar to the one presented in [12]. The microdevice was fabricated using the 0.18 μm CMOS technology from TSMC and is composed of a matrix of 4 × 4 N⁺/P-sub photodiodes, where two photodiodes have 5 μm metal microstructures on top and the other two photodiodes have 20 μm metal microstructures on top [103]. These metal patterns are intended for coarse and fine angle measuring. Each photodiode has its own current-to-frequency converter, with all working in parallel and producing 16 independent pulsed signals. A set of four digital signals controls a digital multiplexer to select only one of the 16 inputs. Figure 21a also shows the block diagram of the readout electronics, while Figure 21b depicts the photograph of the fabricated microdevice [103]. The measurements, performed on two photodetectors, showed the following behavior [103]:

$$\begin{cases} f_{PD1}(\theta) = -0.067\theta^2 + 12.3057\theta + 20.4571 \\ f_{PD2}(\theta) = -0.1002\theta^2 + 4.3276\theta + 682.4571 \end{cases} \quad (16)$$

where θ [degree] is the angle of incidence of light. The laboratory setup used a potentiometer to set the reference voltage from the power supply to $V_{ref} = 1.68$ V. The clock signal, CLK, was produced using a low-cost commercial arbitrary waveform generator, while a Tektronix digital oscilloscope monitored the signal $pulses_{out}$ at the circuit output. A high-power white LED module Thorlabs model MCWHL5 served as the light source. The angle incidence was manually adjusted using a mini-goniometer from Optron featuring scale markings [103]. The conclusion was that the equations $f_{PD1}(\theta)$ and $f_{PD2}(\theta)$ agree well with the measurements (with correlation factors of 97.7% and 94.1%, respectively).

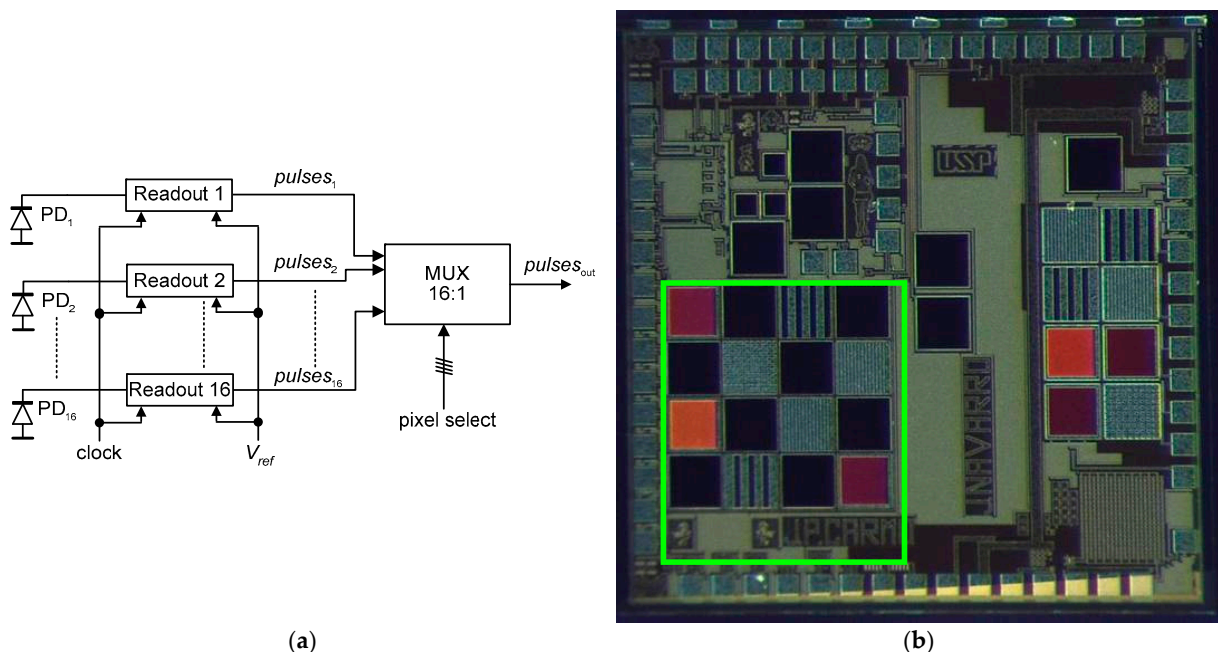


Figure 21. (a) Block diagram of the complete solar tracker, and (b) the photograph of the fabricated microdevice with details of the complete solar tracker developed by Costa et al; the area inside the green box comprises the circuit of solar tracker [103].

Gómez-Merchan et al. introduced a sun sensor architecture that is particularly pertinent due to the rising demands of satellite deployment [153]. Its design leverages photodiodes in the photovoltaic regime instead of the conventional photoconductive mode, enabling zero power consumption for the photoreceptor and facilitating continuous signal generation with logarithmic compression. Integrated with low-power asynchronous digital circuitry for on-chip region of interest (ROI) centroid computation, the sensor was fabricated using the UMC 0.18 μm technology with dimensions of $1516 \mu\text{m} \times 1516 \mu\text{m}$, in continuous mode, and $1318 \mu\text{m} \times 1318 \mu\text{m}$ in time-to-first-spike (TFS) mode. Both modes utilize an array of 64×64 pixels with a pitch of $19.5 \mu\text{m}$, achieving a field of view (FOV) of 88.67° and a resolution of up to 0.98° per pixel. The continuous mode records 5000 measurements per second for 1000 lux, while the TFS mode captures 1000 frames per second. The power consumption is capped at $63 \mu\text{W}$ for the continuous mode and 1.07 mW for the TFS mode, with both modes boasting a dynamic range higher than 100 dB. The continuous mode resolution stands at 1.23° with an accuracy of 2.37° (latitude) and 5.82° (azimuth), whereas the TFS mode presents a higher resolution of 0.0048° and an accuracy of 0.012° (latitude) and 0.043° (azimuth) [153].

Chang et al. from the Space System Research Lab (SSRL) at Korea Aerospace University developed a CMOS sun sensor to determine the incident angle of sunlight. This sensor captures sunlight's projection to calculate the angle [154]. The design comprises a mask with holes in different configurations and diameters that allow sunlight through, positioned at a fixed distance from the sensor. The mask is made of an opaque material, typically silicon, with black-coated SUS306 prototype masks having different hole configurations. The CMOS sensor used is the MT9M112 model by Micron Technology, Inc., which is smaller and consumes less power than CCD sensors, operating within a range of 90 mW to 160 mW, making it ideal for small satellites. The MT9M112 has a resolution of 1280×1024 pixels, measuring $48.35 \text{ mm} \times 83.88 \text{ mm} \times 34.71 \text{ mm}$, and weighing 80.8 g. The digital sun sensor relies on the accurate determination of the projected sunlight's center on the CMOS for precise measurements [154].

Romijn et al. introduces a quadrant sun position sensor developed using silicon carbide (SiC) technology, specifically aimed at overcoming the pitfalls of existing silicon-based sensors that inadvertently react to the Earth's reflected visible light [155]. This new sensor boasts unique quadrant architecture, consisting of four individual photodetectors arranged strategically. These detectors, when combined with a transparent sapphire optical window, function to cast a light spot, facilitating the calculation of direction vectors to the light source. Operating in a field-of-view of $\pm 33^\circ$, this device reaches a minimal mean error of just 1.9° . Furthermore, the tests revealed the sensor's ability to remain "visible blind", meaning it can accurately differentiate UV light sources from regular ambient light conditions. The sensor employs a 0.81 cm^2 photodetector, constructed using 4H-SiC technology aimed at the UV spectral range, and utilizes a pre-coated sapphire optical window. The SiC foundation ensures high UV-to-visible selectivity and enhanced radiation toughness, offering potential for integrated on-chip readout electronics [155]. The same research group developed another sensor constructed from silicon carbide; the sensor integrates wafer-thin 3D optics and boasts a compact design measuring $10 \text{ mm} \times 10 \text{ mm} \times 1 \text{ mm}$ [156]. It delivers a mean angular accuracy of 5.7° within a $\pm 37^\circ$ field-of-view and is equipped with an on-chip temperature sensor, demonstrating sensitivity from 20°C to 200°C . The device operates at a minimal power consumption of $\approx 60 \mu\text{W}$. Its design leverages silicon carbide photodetectors to effectively diminish signal distortions from Earth-reflected light, offering a solution that not only meets satellite miniaturization needs but also anticipates significant cost savings in large-scale production.

Another work by Romijn et al. presents a developed angle-sensitive optical sensor that removes the need for conventional optics [157]. The sensor's design integrates CMOS-compatible diffraction grating layers, allowing for both cost-effective fabrication and significant miniaturization. This approach eliminates the necessity for 3D optic post-processing. The sensor is capable of detecting angular information from a monochromatic

light source across a single axis with a mean absolute accuracy of 0.6° in a $\pm 26^\circ$ field-of-view using just four unique pixels. When it comes to fabrication, the CMOS opto-electronic system used in the sensor's construction leverages in-house BiCMOS technology; a process involving seven lithography masks on 100 mm diameter p-type wafers. Vertical photodetectors, sized at $0.5 \text{ mm} \times 0.5 \text{ mm}$, are utilized, which feature an 8×8 pixel array. The device's angle-sensitive fabrication features a double-diffraction grating stack, which begins with a 2.7 nm oxide layer, followed by layers of titanium nitride (TiN). This TiN layer was chosen due to its low reflectivity properties, which are ideal for the sensor's function.

Koch et al. engineered a sensor for the continuous detection of incoming light angles, fabricated using a standard 250 nm CMOS technology [158]. It employs a simplified design with just two diodes; one shaded and one unshaded. These diodes detect the angle based on the distinct photocurrent ratios produced by them. A feature of this sensor is its compactness, occupying a photo-sensitive area of merely 0.285 mm^2 , while the entire microdevice spans an area of 1.19 mm^2 . The experimental setup of the sensor boasts a precise mechanical construction that can be adjusted to a light source with a remarkable accuracy of one-twelfth of a degree. When evaluating its efficiency, the sensor exhibited accuracy for angles ranging from 0° to 35° . The sensor consumes almost no power when idle and a mere 1 mW during its measurement cycles [158].

Table 5 compares a selected sample of state-of-the-art solar trackers to finish off this section.

Table 5. Comparison of selected state-of-the-art solar trackers.

Ref No.	Fabrication Technology	Photodiodes, Architecture	Key Features	Power Consumption	Other Properties	Purpose Finality
[12]	0.7 μm CMOS (on semiconductor)	4×4 array	Metal microstructures (5 μm , 10 μm)	265 mW, when supplied with 5 V.	Precise solar tracking, scalable design	Angle of solar light incidence
[103]	0.18 μm CMOS (TSMC)	4×4 array	Metal microstructures (5 μm , 20 μm)	Not mentioned	Similar to [12,87], with modified tech/design	Angle of solar light incidence
[153]	UMC 0.18 μm	64×64 pixel	Pinhole	63 μW –1.07 mW	FOV: 88.67° , Resolution: up to $0.98^\circ/\text{pixel}$	Sun sensor for satellite deployment
[154]	Not mentioned (MT9M112 by Micron Technology)	Not mentioned	Mask with different hole configurations	90–160 mW	Resolution: 1280×1024 pixels, Weight: 80.83 g	Determines angle of sunlight
[155]	4H-SiC	Quadrant 2×2 photodetectors	Transparent sapphire optical window	Not mentioned	FOV: $\pm 33^\circ$, Error: 1.9°	Differentiates UV from ambient light
[156]	6 μm 4H-SiC CMOS technology	Not mentioned	Wafer-thin 3D optics	Approx $\pm 60 \mu\text{W}$	FOV: $\pm 37^\circ$, Accuracy: 5.7°	Satellite attitude control
[157]	BiCMOS	8×8 pixel array	Double diffraction grating stack	Not mentioned	FOV: $\pm 26^\circ$, Accuracy: 0.6°	Detects angular information
[158]	250 nm CMOS	Two diodes (shaded unshaded)	Photocurrent ratios	Nearly 0 to 1 mW	Angle Range: $\pm 85^\circ$, high resolution	Continuous detection of light angles

6. Conclusions

This paper presents an overview of optical sensors in CMOS for light measurements in the visible range of the electromagnetic spectrum. Photocurrent conversion was reviewed and the most used types of CMOS photodetectors were also presented. The architectures of photoconversion to current, to voltage, and to frequency were described. A selected set of biomedical and metrology applications were presented and described.

Author Contributions: Conceptualization, J.P.C. and G.M.F.; methodology, R.G., G.M.F. and J.P.C.; validation, R.G., G.M.F. and J.P.C.; writing—original draft preparation, R.G., G.M.F. and M.L.M.A.; supervision, J.P.C.; project administration, J.N.S.J. and J.P.C.; funding acquisition, J.N.S.J. and J.P.C. All authors have read and agreed to the published version of the manuscript.

Funding: This work was partially supported by the FAPESP agency (Fundação de Amparo à Pesquisa do Estado de São Paulo) through the project with the reference number 2019/05248-7. Professor João Paulo Carmo was supported by a PQ scholarship with the reference number CNPq 304312/2020-7.

Conflicts of Interest: The authors declare no conflict of interest.

References

1. Prabhu, S.N.; Gooneratne, C.P.; Mukhopadhyay, S.C. Development of MEMS Sensor for Detection of Creatinine Using MIP Based Approach—A Tutorial Paper. *IEEE Sens. J.* **2021**, *21*, 22170–22181. [[CrossRef](#)]
2. Dean, R.N., Jr.; Luque, A. Applications of Microelectromechanical Systems in Industrial Processes and Services. *IEEE Trans. Ind. Electron.* **2009**, *56*, 913–925. [[CrossRef](#)]
3. Tekin, T. Review of Packaging of Optoelectronic, Photonic, and MEMS Components. *IEEE J. Sel. Top. Quantum Electron.* **2011**, *17*, 704–719. [[CrossRef](#)]
4. Liao, C.D.; Tsai, J.C. The evolution of MEMS displays. *IEEE Trans. Ind. Electron.* **2009**, *56*, 1057–1065. [[CrossRef](#)]
5. Abella, C.S.; Bonina, S.; Cucuccio, A.; D'Angelo, S.; Giustolisi, G.; Grasso, A.D.; Scuderi, A. Autonomous Energy-Efficient Wireless Sensor Network Platform for Home/Office Automation. *IEEE Sens. J.* **2019**, *19*, 3501–3512. [[CrossRef](#)]
6. Liu, J.; Zhao, Z.; Ji, J.; Hu, M. Research and application of wireless sensor network technology in power transmission and distribution system. *Intell. Conver. Netw.* **2020**, *1*, 199–220. [[CrossRef](#)]
7. Lau, P.-Y.; Yung, K.K.-O.; Yung, E.K.-N. A Low-Cost Printed CP Patch Antenna for RFID Smart Bookshelf in Library. *IEEE Trans. Ind. Electron.* **2009**, *57*, 1583–1589. [[CrossRef](#)]
8. Kuo, S.-K.; Chen, S.-L.; Lin, C.-T. Design and Development of RFID Label for Steel Coil. *IEEE Trans. Ind. Electron.* **2009**, *57*, 2180–2186. [[CrossRef](#)]
9. Alahmad, M.A.; Hess, H.L. Evaluation and Analysis of a New Solid-State Rechargeable Microscale Lithium Battery. *IEEE Trans. Ind. Electron.* **2008**, *55*, 3391–3401. [[CrossRef](#)]
10. Chuang, H.S.; Wen, C.M.; Cheng, M.Y.; Chiu, C.H. Automatic vision based optical fiber alignment using multirate technique. *IEEE Trans. Ind. Electron.* **2009**, *56*, 2998–3003. [[CrossRef](#)]
11. Ospina, J.H.; Canuto, E.; Molano, A.; Acuña-Bravo, W. Multilayer control of an optical reference cavity for space applications. *IEEE Trans. Ind. Electron.* **2010**, *57*, 250–2518. [[CrossRef](#)]
12. Costa, J.P.C.; Gounella, R.H.; Bastos, W.B.; Longo, E.; Carmo, J.P. Photovoltaic Sub-Module with Optical Sensor for Angular Measurements of Incident Light. *IEEE Sens. J.* **2019**, *19*, 3111–3120. [[CrossRef](#)]
13. Correia, J.; Bartek, M.; Wolffenbuttel, R. Bulk-micromachined tunable Fabry–Perot microinterferometer for the visible spectral range. *Sens. Actuators A Phys.* **1999**, *76*, 191–196. [[CrossRef](#)]
14. Carmo, J.P.; Rocha, R.P.; Bartek, M.; de Graaf, G.; Wolffenbuttel, R.F.; Correia, J.H. A review of visible-range Fabry–Perot microspectrometers in silicon for the industry. *Opt. Laser Technol.* **2012**, *44*, 2312–2320. [[CrossRef](#)]
15. Wilkins, D.R.; Gallo, L.C.; Costantini, E.; Brandt, W.N.; Blandford, R.D. Light bending and X-ray echoes from behind a supermassive black hole. *Nature* **2021**, *595*, 657–660. [[CrossRef](#)]
16. Zhao, J.; Liu, H.; Deng, L.; Bai, M.; Xie, F.; Wen, S.; Liu, W. High Quantum Efficiency and Broadband Photodetector Based on Graphene/Silicon Nanometer Truncated Cone Arrays. *Sensors* **2021**, *21*, 6146. [[CrossRef](#)]
17. Sukhvasi, S.B.; Sukhvasi, S.B.; Elleithy, K.; Abuzneid, S.; Elleithy, A. CMOS Image Sensors in Surveillance System Applications. *Sensors* **2021**, *21*, 488. [[CrossRef](#)]
18. Green, M.A.; Keevers, M.J. Optical properties of intrinsic silicon at 300 K. *Prog. Photovolt. Res. Appl.* **1995**, *3*, 189–192. [[CrossRef](#)]
19. Wang, H.-T.; Leon-Salas, W.D. An Image Sensor with Joint Sensing and Energy Harvesting Functions. *IEEE Sens. J.* **2014**, *15*, 902–916. [[CrossRef](#)]
20. Huang, C.-C.; Huang, J.K.-T.; Lee, C.-W.; Lin, C.J. A CMOS Active Pixel Sensor with Light Intensity Filtering Characteristics for Image Thresholding Application. *IEEE Sens. J.* **2011**, *12*, 1289–1293. [[CrossRef](#)]
21. Gomes, J.M.; Correia, J.H.; Carmo, J.P. A Low-Cost Flexible-Platform (LCFP) for characterization of photodetectors. *Measurement* **2015**, *61*, 206–215. [[CrossRef](#)]
22. Minas, G.; de Graaf, G.; Wolffenbuttel, R.F.; Correia, J.H. An MCM-based microsystem for colorimetric detection of bio-molecules in biological fluids. *IEEE Sens. J.* **2006**, *6*, 1003–1009. [[CrossRef](#)]
23. Miiikynen, A.J.; Kostamovaara, J.T.; Rahkonen, T.E. CMOS Photodetectors for Industrial Position Sensing. *IEEE Transactions Instrum. Meas.* **1994**, *43*, 489–493. [[CrossRef](#)]
24. Dickinson, A.; Mendis, S.; Inglis, D.; Azadet, K.; Fossum, E. CMOS Digital Camera with Parallel Analog-to-Digital Conversion Architecture. In Proceedings of the IEEE Workshop on Charge Coupled Devices and Advanced Image Sensors, Dana Point, CA, USA, 20–22 April 1995.
25. Dickinson, A.; Ackland, B.; Ed, E.S.; Inglis, D.; Fossum, E.R. A 256 × 256 CMOS Active Pixel image Sensor with Motion Detection. In Proceedings of the IEEE Solid State Circuits Conference ISSCC95, San Francisco, CA, USA, 15–17 February 1995.
26. Biber, A.; Seitz, P.; Jackel, H. Avalanche photodiode image sensor in standard BiCMOS technology. *IEEE Trans. Electron Devices* **2000**, *47*, 2241–2243. [[CrossRef](#)]

27. Pimenta, S.; Carmo, J.P.; Correia, R.G.; Minas, G.; Castanheira, E.M.S. Characterization of silicon photodiodes for diffuse reflectance signal extraction. In Proceedings of the 2015 IEEE 4th Portuguese Meeting on Bioengineering, Porto, Portugal, 26–28 February 2015.
28. Moini, A. *Vision Chips*; Kluwer Academic Publishers: Norwell, MA, USA, 2000.
29. Correia, R.G.; Pimenta, S.; Minas, G. CMOS Integrated Photodetectors and Light-to-Frequency Converters for Spectro-photometric Measurements. *IEEE Sens. J.* **2017**, *17*, 3438–3445. [[CrossRef](#)]
30. Ferreira, G.M.; Silva, V.; Minas, G.; Catarino, S.O. Simulation Study of Vertical p–n Junction Photodiodes' Optical Performance According to CMOS Technology. *Appl. Sci.* **2022**, *12*, 2580. [[CrossRef](#)]
31. Minas, G.; Ribeiro, J.C.; Wolffenbuttel, R.F.; Correia, J.H. On-chip integrated CMOS optical detection microsystem for spectrophotometric analyses in biological microfluidic systems. In Proceedings of the IEEE International Symposium on Industrial Electronics, Dubrovnik, Croatia, 20–23 June 2005; Volume 3, pp. 1133–1138.
32. Chuah, J.H.; Holburn, D. An integrated solid-state solution for secondary electron detection. *Analog. Integr. Circuits Signal Process.* **2013**, *79*, 395–411. [[CrossRef](#)]
33. Koklu, G.; Etienne-Cummings, R.; Leblebici, Y.; De Micheli, G.; Carrara, S. Characterization of standard CMOS compatible photodiodes and pixels for Lab-on-Chip devices. In Proceedings of the 2013 IEEE International Symposium on Circuits and Systems, Beijing, China, 19–23 May 2013; pp. 1075–1078.
34. Rocha, R.P.; Maciel, M.J.; Gomes, J.M.; Correia, J.H.; Carmo, J.P. The effect of microlenses in photodiodes' dark current measurement. In Proceedings of the 2014 Science and Information Conference (SAI), London, UK, 27–29 August 2014.
35. Correia, J.; de Graaf, G.; Bartek, M.; Wolffenbuttel, R. A single-chip CMOS optical microspectrometer with light-to-frequency converter and bus interface. *IEEE J. Solid-State Circuits* **2002**, *37*, 1344–1347. [[CrossRef](#)]
36. Bielecki, Z.; Achtenberg, K.; Kopytko, M.; Mikołajczyk, J.; Wojtas, J.; Rogalski, A. Review of photodetectors characterization methods. *Bull. Pol. Acad. Sci. Tech. Sci.* **2022**, *70*, 140534. [[CrossRef](#)]
37. Teranishi, N. Analysis of Subthreshold Current Reset Noise in Image Sensors. *Sensors* **2016**, *16*, 663. [[CrossRef](#)]
38. Chen, Y.; Wang, X.; Mierop, A.J.; Theuwsen, A.J.P. A CMOS Image Sensor with In-Pixel Buried-Channel Source Follower and Optimized Row Selector. *IEEE Trans. Electron Devices* **2009**, *56*, 2390–2397. [[CrossRef](#)]
39. Lee, T.-H.; Cho, G.; Kim, H.J.; Lee, S.W.; Lee, W.; Han, S.H. Analysis of 1/f Noise in CMOS Pre-amplifier with CDS Circuit. *IEEE Trans. Nucl. Sci.* **2002**, *49*, 1819–1823.
40. Huang, W.; Xu, Z. Characteristics and Performance of Image Sensor Communication. *IEEE Photonics J.* **2017**, *9*, 7902919. [[CrossRef](#)]
41. Li, J.; Li, J.; Zhou, S.; Yi, F. Metasurface Photodetectors. *Micromachines* **2021**, *12*, 1584. [[CrossRef](#)] [[PubMed](#)]
42. Li, J.; Bao, L.; Jiang, S.; Guo, Q.; Xu, D.; Xiong, B.; Zhang, G.; Yi, F. Inverse design of multifunctional plasmonic metamaterial absorbers for infrared polarimetric imaging. *Opt. Express* **2019**, *27*, 8375–8386. [[CrossRef](#)] [[PubMed](#)]
43. Jiang, S.; Li, J.; Li, J.; Zhang, G.; Liu, H.; Yi, F. Genetic optimization of plasmonic metamaterial absorber towards dual-band infrared imaging polarimetry. *Opt. Express* **2020**, *28*, 22617–22629. [[CrossRef](#)] [[PubMed](#)]
44. Bukhari, S.S.; Vardaxoglou, J.Y.; Whittow, W. A Metasurfaces Review: Definitions and Applications. *Appl. Sci.* **2019**, *9*, 2727. [[CrossRef](#)]
45. Novotny, L.; van Hulst, N. Antennas for Light. *Nat. Photonics* **2011**, *5*, 83–90. [[CrossRef](#)]
46. Yoon, G.; Kim, I.; Rho, J. Microelectronic engineering challenges in fabrication towards realization of practical metamaterials. *Microelectron. Eng.* **2016**, *163*, 7–20. [[CrossRef](#)]
47. Meinzer, N.; Barnes, W.L.; Hooper, I.R. Plasmonic meta-atoms and metasurfaces. *Nat. Photonics* **2014**, *8*, 889–898. [[CrossRef](#)]
48. Bharadwaj, P.; Deutsch, B.; Novotny, L. Optical Antennas. *Adv. Opt. Photonics* **2009**, *1*, 438–483. [[CrossRef](#)]
49. Cao, L.; Park, J.-S.; Fan, P.; Clemens, B.; Brongersma, M.L. Resonant Germanium Nanoantenna Photodetectors. *Nano Lett.* **2010**, *10*, 1229–1233. [[CrossRef](#)]
50. Ebbesen, T.W.; Lezec, H.J.; Ghaemi, H.F.; Thio, T.; Wolff, P.A. Extraordinary optical transmission through sub-wavelength hole arrays. *Nature* **1998**, *391*, 667–669. [[CrossRef](#)]
51. Agranov, G.; Gilton, T.; Mauritzson, R.; Boettiger, U.; Altice, P.; Shah, J.; Ladd, J.; Fan, X.; Brady, F.; McKee, J.; et al. Optical-electrical characteristics of small, sub-4 μm and sub-3 μm pixels for modern CMOS Image Sensors. In Proceedings of the IEEE Workshop on CCDs and Advanced Image Sensors, R31, Karuizawa, Japan, 9–11 June 2005; pp. 206–209.
52. Pal, T.; Arif, M.; I Khondaker, S. High performance organic phototransistor based on regioregular poly(3-hexylthiophene). *Nanotechnology* **2010**, *21*, 325201. [[CrossRef](#)] [[PubMed](#)]
53. Esmaeili-Rad, M.R.; Papadopoulos, N.P.; Bauza, M.; Nathan, A.; Wong, W.S. Blue-light-sensitive phototransistor for indirect X-ray image sensors. *IEEE Electron Device Lett.* **2012**, *33*, 567–569. [[CrossRef](#)]
54. Abdolahad, M.; Taghinejad, H.; Saeidi, A.; Taghinejad, M.; Janmaleki, M.; Mohajerzadeh, S. Cell membrane electrical charge investigations by silicon nanowires incorporated field effect transistor (SiNWFET) suitable in cancer research. *RSC Adv.* **2013**, *4*, 7425–7431. [[CrossRef](#)]
55. Taghinejad, M.; Taghinejad, H.; Ganji, M.; Rostamian, A.; Mohajerzadeh, S.; Abdolahad, M.; Kolahdouz, M. Integration of Ni₂Si/Si Nanograin Heterojunction on n-MOSFET to Realize High-Sensitivity Phototransistors. *IEEE Trans. Electron Devices* **2014**, *61*, 3239–3244. [[CrossRef](#)]
56. Li, W.; Valentine, J.G. Harvesting the loss: Surface plasmon-based hot electron photodetection. *Nanophotonics* **2016**, *6*, 177–191. [[CrossRef](#)]

57. Taghinejad, M.; Xu, Z.; Lee, K.-T.; Lian, T.; Cai, W. Transient Second-Order Nonlinear Media: Breaking the Spatial Symmetry in the Time Domain via Hot-Electron Transfer. *Phys. Rev. Lett.* **2020**, *124*, 013901. [CrossRef]
58. Knight, M.W.; Sobhani, H.; Nordlander, P.; Halas, N.J. Photodetection with Active Optical Antennas. *Science* **2011**, *332*, 702–704. [CrossRef]
59. Taghinejad, M.; Cai, W. All-Optical Control of Light in Micro- and Nanophotonics. *ACS Photonics* **2019**, *6*, 1082–1093. [CrossRef]
60. Taghinejad, M.; Xia, C.; Hrton, M.; Lee, K.-T.; Kim, A.S.; Li, Q.; Guzelturk, B.; Kalousek, R.; Xu, F.; Cai, W.; et al. Determining hot-carrier transport dynamics from terahertz emission. *Science* **2023**, *382*, 299–305. [CrossRef] [PubMed]
61. Boyle, W.S.; Smith, G.E. Charge Coupled Semiconductor Devices. *Bell Syst. Tech. J.* **1970**, *49*, 587–593. [CrossRef]
62. Boyle, W.S.; Smith, G.E. Buried Channel Charge Coupled Devices. U.S. Patent 3,792,322 (US3792322A), 12 February 1974.
63. Boyle, W.S.; Smith, G.E. Three Dimensional Charge Coupled Devices. U.S. Patent 3,796,927 (US3796927), 12 March 1974.
64. Gerstner, E. Nobel Prize 2009: Kao, Boyle & Smith. *Nat. Phys.* **2009**, *5*, 780. [CrossRef]
65. Faramarzpour, N.; El-Desouki, M.; Deen, M.J.; Fang, Q.; Shahramshirani; Liu, L. CMOS imaging for biomedical applications. *IEEE Potentials* **2008**, *27*, 31–36. [CrossRef]
66. Litwiller, D. CCD vs. CMOS: Facts and fiction. *Photonics Spectra* **2001**, *35*, 154–158.
67. Powell, K.; Chana, D.; Fish, D.; Thompson, C. Restoration and frequency analysis of smeared CCD images. *Appl. Opt.* **1999**, *38*, 1343–1347. [CrossRef]
68. Gamal, A.E.; Eltoukhy, H. CMOS Image Sensors. *IEEE Circuits Devices Mag.* **2005**, *21*, 6–20. [CrossRef]
69. Hamamatsu Photonics K.K. CCD Image Sensors. Technical Note, KMPDC0036EB, November 2020; pp. 1–39. Available online: https://www.hamamatsu.com/content/dam/hamamatsu-photonics/sites/documents/99_SALES_LIBRARY/ssd/ccd_kmpd9002e.pdf (accessed on 1 February 2024).
70. HORIBA Jobin Yvon, SynapseTM CCD, CCD-512x512-BIUV Datasheet. 2006, pp. 1–4. Available online: https://static.horiba.com/fileadmin/Horiba/Products/Scientific/Optical_Components_and_OEM/Spectroscopy_Cameras/CCD_Cameras/Synapse_BIUV_512x512_Scientific_CCD_Camera.pdf (accessed on 1 February 2024).
71. Freitas, L.M.C.; Dias, F.M. Design Improvements on Fast, High-Order, Incremental Sigma-Delta ADCs for Low-Noise Stacked CMOS Image Sensors. *Electronics* **2021**, *10*, 1936. [CrossRef]
72. Rahman, H.; Sejan, M.A.S.; Kim, J.-J.; Chung, W.-Y. Reduced Tilting Effect of Smartphone CMOS Image Sensor in Visible Light Indoor Positioning. *Electronics* **2020**, *9*, 1635. [CrossRef]
73. Wei, J.; Li, X.; Sun, L.; Li, D. A Low-Power Column-Parallel Gain-Adaptive Single-Slope ADC for CMOS Image Sensors. *Electronics* **2020**, *9*, 757. [CrossRef]
74. Cahyadi, W.A.; Chung, Y.H.; Ghassemlooy, Z.; Hassan, N.B. Optical Camera Communications: Principles, Modulations, Potential and Challenges. *Electronics* **2020**, *9*, 1339. [CrossRef]
75. Cheng, H.-Y.; King, Y.-C. An ultra-low dark current CMOS image sensor cell using n/sup +/ ring reset. *IEEE Electron Device Lett.* **2002**, *23*, 538–540. [CrossRef]
76. Freitas, L.M.C.; Morgado-Dias, F. Reference Power Supply Connection Scheme for Low-Power CMOS Image Sensors Based on Incremental Sigma-Delta Converters. *Electronics* **2021**, *10*, 299. [CrossRef]
77. Dyck, R.; Weckler, G. Integrated arrays of silicon photodetectors for image sensing. *IEEE Trans. Electron Devices* **1968**, *15*, 196–201. [CrossRef]
78. Hoekstra, W.; van der Avoird, A.; Kole, M.; Schrooten, G.G.; Schaeffer, C.J. A memory read-out approach for a 0.5 μm CMOS image sensor. *Proc. SPIE* **1998**, *3301*, 151–157.
79. Fujimori, I.L.; Wang, C.-C.; Sodini, C.G. A 256 \times 256 CMOS Differential Passive Pixel Image with FPN Reduction Techniques. *IEEE J. Solid-State Circuits* **2000**, *35*, 2031–2037. [CrossRef]
80. Kozłowski, L.J.; Luo, J.; Kleinhans, W.E.; Liu, T. Comparison of Passive and Active Pixel Schemes for CMOS Visible Imagers. *Proc. SPIE* **1998**, *3360*, 101–110.
81. Carmo, J.; Silva, M.; Rocha, R.; Ribeiro, J.; Goncalves, L.; Correia, J. Stereoscopic image sensor in CMOS technology. *Procedia Eng.* **2011**, *25*, 1277–1280. [CrossRef]
82. El-Desouki, M.; Deen, M.J.; Fang, Q.; Liu, L.; Tse, F.; Armstrong, D. CMOS Image Sensors for High Speed Applications. *Sensors* **2009**, *9*, 430–444. [CrossRef]
83. Takahashi, H.; Kinoshita, M.; Morita, K.; Shirai, T.; Sato, T.; Kimura, T.; Yuzurihara, H.; Inoue, S.; Matsumoto, S. A 3.9 μm pixel pitch VGA format 10 b digital output CMOS image sensor with 1.5 transistor/pixel. *IEEE J. Solid State Circuits* **2004**, *39*, 2417–2424. [CrossRef]
84. Mori, M.; Katsuno, M.; Kasuga, S.; Murata, T.; Yamaguchi, T. 1/4 Inch 2 Mpixel MOS image sensor with 1.75 transistors/pixel. *IEEE J. Solid State Circuits* **2004**, *39*, 2426–2430. [CrossRef]
85. Tarabsheh, A.A.; Alheeh, J. Design and Simulation of a 3-Transistor Active Pixel Sensor Using MATLAB Simulink. In Proceedings of the 2022 International Arab Conference on Information Technology (ACIT), Abu Dhabi, United Arab Emirates, 22–24 November 2022; pp. 1–4.
86. Karim, K.; Nathan, A.; Rowlands, J. Amorphous silicon active pixel sensor readout circuit for digital imaging. *IEEE Trans. Electron Devices* **2003**, *50*, 200–208. [CrossRef]
87. Santos, P.M.; Monteiro, D.W.L.; Salles, L.P. Current-Mode Self-Amplified CMOS Sensor Intended for 2D Temperature Microgradients Measurement and Imaging. *Sensors* **2020**, *20*, 5111. [CrossRef] [PubMed]

88. Belmonte, P.N.A.; Abecassis, U.V.; Chaves, L.; Salles, L.P.; Monteiro, D.W.d.L. A high performance integrated readout circuit for wavefront sensors. *SN Appl. Sci.* **2020**, *2*, 1816–1825. [[CrossRef](#)]
89. Brunetti, A.M.; Choubey, B. A Low Dark Current 160 dB Logarithmic Pixel with Low Voltage Photodiode Biasing. *Electronics* **2021**, *10*, 1096. [[CrossRef](#)]
90. Minas, G.; Wolffenbuttel, R.F.; Correia, J.H. A lab-on-a-chip for spectrophotometric analysis of biological fluids. *Lab A Chip* **2005**, *5*, 1303–1309. [[CrossRef](#)]
91. Snoeij, M.F.; Theuwissen, A.J.P.; Makinwa, K.A.A.; Huijsing, J.H. Multiple-Ramp Column-Parallel ADC Architectures for CMOS Image Sensors. *IEEE J. Solid-State Circuits* **2007**, *42*, 2968–2977. [[CrossRef](#)]
92. Yang, Y.; Li, Z.; Liu, M.; Liu, W.; Li, Z.; Hou, Y.; Liu, X.; Wang, X.; Liu, Y. Design of a Wide-Range and High-Precision Analog Front-End Circuit for Multi-Parameter Sensors. *Electronics* **2023**, *12*, 2962. [[CrossRef](#)]
93. Xu, J.; Wang, Y.; Wu, M.; Zhang, R.; Wei, S.; Zhang, G.; Yang, C.-F. A High-Accuracy Ultra-Low-Power Offset-Cancellation On-Off Bandgap Reference for Implantable Medical Electronics. *Electronics* **2019**, *8*, 814. [[CrossRef](#)]
94. Snoeij, M.F.; Theuwissen, A.J.P.; Makinwa, K.A.A.; Huijsing, J.H. A CMOS Imager with Column-Level ADC Using Dynamic Column Fixed-Pattern Noise Reduction. *IEEE J. Solid-State Circuits* **2006**, *41*, 3007–3015. [[CrossRef](#)]
95. Zhang, T.; Li, X.; Li, J.; Xu, Z. CMOS Fixed Pattern Noise Removal Based on Low Rank Sparse Variational Method. *Appl. Sci.* **2020**, *10*, 3694. [[CrossRef](#)]
96. Yue, X.; Fossum, E.R. Design and Characterization of a Burst Mode 20 Mfps Low Noise CMOS Image Sensor. *Sensors* **2023**, *23*, 6356. [[CrossRef](#)] [[PubMed](#)]
97. Klosowsky, M.; Sun, Y. Fixed Pattern Noise Reduction and Linearity Improvement in Time-Mode CMOS Image Sensors. *Sensors* **2020**, *20*, 5921. [[CrossRef](#)] [[PubMed](#)]
98. Zhang, T.; Li, X.; Li, J.; Xu, Z. CMOS Fixed Pattern Noise Elimination Based on Sparse Unidirectional Hybrid Total Variation. *Sensors* **2020**, *20*, 5567. [[CrossRef](#)] [[PubMed](#)]
99. Rocha, J.G.; Minas, G.; Lanceros-Mendez, S. Pixel Readout Circuit for X-Ray Imagers. *IEEE Sens. J.* **2010**, *10*, 1740–1745. [[CrossRef](#)]
100. Carmo, J.P.; Gounella, R.H.; Costa, J.P.; Nordi, T.M. Microelectronics Research at USP of São Carlos. User Stories on Prototyped Design. OnSemi C0.7 Section. Europractice Activity Report 2018–2019. 2018, p. 16. Available online: <https://europractice-ic.com/wp-content/uploads/2019/06/EP-activity-Report-2018.pdf> (accessed on 14 January 2024).
101. Zhang, X.; Leomant, S.; Lau, K.L.; Bermak, A. A Compact Digital Pixel Sensor (DPS) Using 2T-DRAM. *J. Low Power Electron. Appl.* **2011**, *1*, 77–96. [[CrossRef](#)]
102. Hassanli, K.; Seyed, S.M.; Dehghani, R.; Jalili, A.; Wilkner, J.J. A highly sensitive, low-power, and wide dynamic range CMOS digital pixel sensor. *Sens. Actuators A* **2015**, *236*, 82–91. [[CrossRef](#)]
103. Costa, J.P.C.; Gounella, R.H.; Granado, T.C.; Machado, R.T.; Assagra, Y.A.O.; Correia, J.H.; Carmo, J.P. Optical CMOS sensor for angular measurements with readout electronics. In Proceedings of the 32nd Symposium on Microelectronics Technology and Devices (SBMicro 2017), Fortaleza, CE, Brazil, 28 August–1 September 2017.
104. Wojtyna, R. Low-voltage quasi-linear current-to-voltage converter for analog signal processing. In Proceedings of the 2016 MIXDES—23rd International Conference “Mixed Design of Integrated Circuits and Systems, Lodz, Poland, 23–25 June 2016; pp. 405–409. [[CrossRef](#)]
105. Srinivasan, V.; Chawla, R.; Hasler, P. Linear current-to-voltage and voltage-to-current converters. In Proceedings of the 48th Midwest Symposium on Circuits and Systems, Covington, KY, USA, 7–10 August 2005; pp. 675–678.
106. Chodavarapu, V.; Bukowski, R.; Titus, A.; Cartwright, A.; Bright, F. CMOS integrated luminescence oxygen multi-sensor system. *Electron. Lett.* **2007**, *43*, 688–689. [[CrossRef](#)]
107. Correia, J.; de Graaf, G.; Bartek, M.; Wolffenbuttel, R. A CMOS optical microspectrometer with light-to-frequency converter, bus interface, and stray-light compensation. *IEEE Trans. Instrum. Meas.* **2001**, *50*, 1530–1537. [[CrossRef](#)]
108. Kuo, W.-C.; Chiang, C.-T.; Huang, Y.-C. An Automatic Light Monitoring System with Light-to-Frequency Converter for Flower Planting. In Proceedings of the IEEE Instrumentation and Measurement Technology Conference, Victoria, BC, Canada, 12–15 May 2008; pp. 1146–1149. [[CrossRef](#)]
109. de Graaf, G.; Wolffenbuttel, R. Light-to-frequency converter using integrating mode photodiodes. *IEEE Trans. Instrum. Meas.* **1997**, *46*, 933–936. [[CrossRef](#)]
110. Ferreira, G.M.; Baptista, V.; Silva, V.; Veiga, M.I.; Minas, G.; Catarino, S.O. CMOS Spectrophotometric Microsystem for Malaria Detection. *IEEE Trans. Biomed. Eng.* **2023**, *70*, 2318–2328. [[CrossRef](#)]
111. Frohmader, K.P. A Novel MOS Compatible Light Intensity-to-Frequency Converter Suited for Monolithic Integration. *IEEE J. Solid-State Circuits* **1982**, *17*, 588–591. [[CrossRef](#)]
112. Yu, B.; Lo, J.Y.; Kuech, T.F.; Palmer, G.M.; Bender, J.E.; Ramanujam, N. Cost-effective diffuse reflectance spectroscopy device for quantifying tissue absorption and scattering in vivo. *J. Biomed. Opt.* **2008**, *13*, 060505. [[CrossRef](#)] [[PubMed](#)]
113. Lo, J.Y.; Yu, B.; Fu, H.L.; Bender, J.E.; Palmer, G.M.; Kuech, T.F.; Ramanujam, N. A strategy for quantitative spectral imaging of tissue absorption and scattering using light emitting diodes and photodiodes. *Opt. Express* **2009**, *17*, 1372–1384. [[CrossRef](#)] [[PubMed](#)]
114. Georgakoudi, I.; Jacobson, B.C.; Van Dam, J.; Backman, V.; Wallace, M.B.; Müller, M.G.; Zhang, Q.; Badizadegan, K.; Sun, D.; Thomas, G.A.; et al. Fluorescence, reflectance, and light-scattering spectroscopy for evaluating dysplasia in patients with Barrett’s esophagus. *Gastroenterology* **2001**, *120*, 1620–1629. [[CrossRef](#)] [[PubMed](#)]

115. Gounella, R.H.; Costa, J.P.C.; Granado, T.C.; Assagra, Y.A.O.; Carmo, J.P. CMOS developments for photonic modules on endoscopic capsules. In Proceedings of the 2017 SBMO/IEEE MTT-S International Microwave and Optoelectronics Conference (IMOC), Aguas de Lindoia, Brazil, 27–30 August 2017; pp. 1–4. [\[CrossRef\]](#)
116. Ferreira, D.S.; Mirkovic, J.; Wolffenbuttel, R.F.; Correia, J.H.; Feld, M.S.; Minas, G. Narrow-band pass filter array for integrated opto-electronic spectroscopy detectors to assess esophageal tissue. *Biomed. Opt. Express* **2011**, *2*, 1703–1716. [\[CrossRef\]](#) [\[PubMed\]](#)
117. Pirnstill, C.W.; Coté, G.L. Malaria Diagnosis Using a Mobile Phone Polarized Microscope. *Sci. Rep.* **2015**, *5*, 13368. [\[CrossRef\]](#) [\[PubMed\]](#)
118. Catarino, S.O.; Felix, P.; Sousa, P.J.; Pinto, V.; Veiga, M.I.; Minas, G. Portable Device for Optical Quantification of Hemozoin in Diluted Blood Samples. *IEEE Trans. Biomed. Eng.* **2019**, *67*, 365–371. [\[CrossRef\]](#) [\[PubMed\]](#)
119. Yadav, S.; Khanam, R.; Singh, J. A purview into highly sensitive magnetic SERS detection of hemozoin biomarker for rapid malaria diagnosis. *Sens. Actuators B Chem.* **2021**, *355*, 131303. [\[CrossRef\]](#)
120. McBirney, S.E.; Chen, D.; Scholtz, A.; Ameri, H.; Armani, A.M. Rapid Diagnostic for Point-of-Care Malaria Screening. *ACS Sensors* **2018**, *3*, 1264–1270. [\[CrossRef\]](#)
121. Giacometti, M.; Pravettoni, T.; Barsotti, J.; Milesi, F.; Figares, C.d.O.; Maspero, F.; Coppadoro, L.P.; Benevento, G.; Ciardo, M.; Alano, P.; et al. Impedance-Based Rapid Diagnostic Tool for Single Malaria Parasite Detection. *IEEE Trans. Biomed. Circuits Syst.* **2022**, *16*, 1325–1336. [\[CrossRef\]](#) [\[PubMed\]](#)
122. Rifaie-Graham, O.; Pollard, J.; Raccio, S.; Balog, S.; Rusch, S.; Hernández-Castañeda, M.A.; Mantel, P.-Y.; Beck, H.-P.; Bruns, N. Hemozoin-catalyzed precipitation polymerization as an assay for malaria diagnosis. *Nat. Commun.* **2019**, *10*, 1369. [\[CrossRef\]](#) [\[PubMed\]](#)
123. Raccio, S.; Pollard, J.; Djuhadi, A.; Balog, S.; Pellizzoni, M.M.; Rodriguez, K.J.; Rifaie-Graham, O.; Bruns, N. Rapid quantification of the malaria biomarker hemozoin by improved biocatalytically initiated precipitation atom transfer radical polymerizations. *Analyst* **2020**, *145*, 7741–7751. [\[CrossRef\]](#) [\[PubMed\]](#)
124. Review of X-ray detection systems. *Opto-Electron. Rev.* **2024**, *31*, 1–8. [\[CrossRef\]](#)
125. Anissi, H.D.; Geibel, M.A. Intraoral Radiology in General Dental Practices—A Comparison of Digital and Film-Based X-Ray Systems with Regard to Radiation Protection and Dose Reduction. *RöFo-Fortschritte Auf Dem Geb. Rönt-Genstrahlen Bildgeb. Verfahr.* **2014**, *186*, 762–767. [\[CrossRef\]](#) [\[PubMed\]](#)
126. Ansari, S.; Bianconi, S.; Kang, C.; Mohseni, H. From Material to Cameras: Low-Dimensional Photodetector Arrays on CMOS. *Small Methods* **2023**, e2300595. [\[CrossRef\]](#)
127. Dodd, P.E.; Shaneyfelt, M.R.; Schwank, J.R.; Felix, J.A. Current and Future Challenges in Radiation Effects on CMOS Electronics. *IEEE Trans. Nucl. Sci.* **2010**, *57*, 1747–1763. [\[CrossRef\]](#)
128. Rocha, J.; Ramos, N.; Lanceros-Mendez, S.; Wolffenbuttel, R.; Correia, J. CMOS X-rays detector array based on scintillating light guides. *Sens. Actuators A Phys.* **2004**, *110*, 119–123. [\[CrossRef\]](#)
129. The Roditi International Corporation. CsI(Tl)–Thallium Doped Caesium Iodide. Available online: https://www.roditi.com/scintillators/CsI_Tl.htm (accessed on 1 February 2024).
130. Hilger Crystals. Thallium Doped Caesium Iodide. Available online: <https://www.hilger-crystals.co.uk/materials/thallium-doped-caesium-iodide/> (accessed on 9 November 2023).
131. Cha, B.K.; Shin, J.-H.; Bae, J.H.; Lee, C.-H.; Chang, S.; Kim, H.K.; Kim, C.K.; Cho, G. Scintillation characteristics and imaging performance of CsI:Tl thin films for X-ray imaging applications. *Nucl. Instruments Methods Phys. Res. Sect. A Accel. Spectrometers Detect. Assoc. Equip.* **2009**, *604*, 224–228. [\[CrossRef\]](#)
132. Hangzhou Shalom Electro-optics Technology Co., Ltd. CsI(Tl) Arrays, Thallium Doped Cesium Iodide, Csi Tl Detector, Csi Detector, Csi Tl Crystal. Available online: <https://www.shalomeo.com/Scintillators/CsI-Tl-Arrays/product-373.html> (accessed on 9 November 2023).
133. Rocha, J.; Correia, J. A high-performance scintillator-silicon-well X-ray microdetector based on DRIE techniques. *Sens. Actuators A Phys.* **2001**, *92*, 203–207. [\[CrossRef\]](#)
134. Lu, L.; Sun, M.; Lu, Q.; Wu, T.; Huang, B. High energy X-ray radiation sensitive scintillating materials for medical imaging, cancer diagnosis and therapy. *Nano Energy* **2020**, *79*, 105437. [\[CrossRef\]](#)
135. Yagi, N.; Yamamoto, M.; Uesugi, K.; Inoue, K. A large-area CMOS imager as an X-ray detector for synchrotron radiation experiments. *J. Synchrotron Radiat.* **2004**, *11*, 347–352. [\[CrossRef\]](#) [\[PubMed\]](#)
136. Alzahrani, H.; Richards, S.; Sedgwick, I.; Seller, P.; Konstantinidis, A.; Royle, G.; Ricketts, K. Image quality determination of a novel digital detector for X-ray imaging and cone-beam computed tomography applications. *Nucl. Instruments Methods Phys. Res. Sect. A Accel. Spectrometers Detect. Assoc. Equip.* **2020**, *968*, 163914. [\[CrossRef\]](#)
137. Desjardins, K.; Medjoubi, K.; Sacchi, M.; Popescu, H.; Gaudemer, R.; Belkhou, R.; Stanescu, S.; Swaraj, S.; Besson, A.; Vijayakumar, J.; et al. Backside-illuminated scientific CMOS detector for soft X-ray resonant scattering and ptychography. *J. Synchrotron Radiat.* **2020**, *27*, 1577–1589. [\[CrossRef\]](#)
138. Son, S.-Y.; Choi, K.-W.; Kim, J.-M.; Jeong, H.-W.; Kwon, K.-T.; Cho, J.-H.; Lee, J.-H.; Jung, J.-Y.; Kim, K.-W.; Lee, Y.-A.; et al. Evaluation of Image Quality for Various Electronic Portal Imaging Devices in Radiation Therapy*. *J. Radiol. Sci. Technol.* **2015**, *38*, 451–461. [\[CrossRef\]](#)

139. Konstantinidis, A.C.; Szafraniec, M.B.; Speller, R.D.; Olivo, A. The Dexela 2923 CMOS X-ray detector: A flat panel detector based on CMOS active pixel sensors for medical imaging applications. *Nucl. Instrum. Methods Phys. Res. Sect. A Accel. Spectrometers Detect. Assoc. Equip.* **2012**, *689*, 12–21. [[CrossRef](#)]
140. Scheuermann, J.R.; Howansky, A.; Hansroul, M.; Léveillé, S.; Tanioka, K.; Zhao, W. Toward Scintillator High-Gain Avalanche Rushing Photoconductor Active Matrix Flat Panel Imager (SHARP-AMFPI): Initial fabrication and characterization. *Med. Phys.* **2017**, *45*, 794–802. [[CrossRef](#)] [[PubMed](#)]
141. Minas, G.; Martins, J.; Ribeiro, J.; Wolffenbuttel, R.; Correia, J. Biological microsystem for measuring uric acid in biological fluids. *Sens. Actuators A Phys.* **2004**, *110*, 33–38. [[CrossRef](#)]
142. Norian, H.; Kymissis, I.; Shepard, K.L. Integrated CMOS quantitative polymerase chain reaction lab-on-chip. In Proceedings of the 2013 Symposium on VLSI Circuits, Kyoto, Japan, 12–14 June 2013; pp. C220–C221.
143. Manaresi, N.; Romani, A.; Medoro, G.; Altomare, L.; Leonardi, A.; Tartagni, M.; Guerrieri, R. A cmos chip for individual cell manipulation and detection. *IEEE J. Solid-State Circuits* **2003**, *38*, 2297–2305. [[CrossRef](#)]
144. Lee, L.M.; Cui, X.; Yang, C. The application of on-chip optofluidic microscopy for imaging *Giardia lamblia* trophozoites and cysts. *Biomed. Microdevices* **2009**, *11*, 951–958. [[CrossRef](#)] [[PubMed](#)]
145. Shen, L.; Ratterman, M.; Klotzkin, D.; Papautsky, I. A CMOS optical detection system for point-of-use luminescent oxygen sensing. *Sens. Actuators B Chem.* **2011**, *155*, 430–435. [[CrossRef](#)]
146. Hu, C.; Annese, V.F.; Velugotla, S.; Al-Rawhani, M.; Cheah, B.C.; Grant, J.; Barrett, M.P.; Cumming, D.R.S. Disposable Paper-on-CMOS Platform for Real-Time Simultaneous Detection of Metabolites. *IEEE Trans. Biomed. Eng.* **2020**, *67*, 2417–2426. [[CrossRef](#)] [[PubMed](#)]
147. Wang, S.; Zhao, X.; Khimji, I.; Akbas, R.; Qiu, W.; Edwards, D.; Cramer, D.W.; Ye, B.; Demirci, U. Integration of cell phone imaging with microchip ELISA to detect ovarian cancer HE4 biomarker in urine at the point-of-care. *Lab A Chip* **2011**, *11*, 3411–3418. [[CrossRef](#)] [[PubMed](#)]
148. Nieuwenhuis, J.; Bastemeijer, J.; Bossche, A.; Vellekoop, M. Near-field optical sensors for particle shape measurements. *IEEE Sens. J.* **2003**, *3*, 646–651. [[CrossRef](#)]
149. Wu, J.; Liu, X.; Wang, L.; Dong, L.; Pu, Q. An economical fluorescence detector for lab-on-a-chip devices with a light emitting photodiode and a low-cost avalanche photodiode. *Analyst* **2011**, *137*, 519–525. [[CrossRef](#)]
150. Pinto, V.; Araújo, C.; Sousa, P.; Gonçalves, L.; Minas, G. A low-cost lab-on-a-chip device for marine pH quantification by colorimetry. *Sens. Actuators B Chem.* **2019**, *290*, 285–292. [[CrossRef](#)]
151. Li, H.; Li, Q.; Wang, X.; Xu, K.; Chen, Z.; Gong, X.; Liu, X.; Tong, L.; Tang, B. Simultaneous Determination of Superoxide and Hydrogen Peroxide in Macrophage RAW 264.7 Cell Extracts by Microchip Electrophoresis with Laser-Induced Fluorescence Detection. *Anal. Chem.* **2009**, *81*, 2193–2198. [[CrossRef](#)]
152. Carmo, J.P.; Gounella, R.H.; Costa, J.P. Analog and Digital IP Blocks for Platforms of Sensors. User Stories on Prototyped Design. OnSemi C0.7 Section, Europractice Activity Report 2017; p. 21. Available online: <https://europractice-ic.com/wp-content/uploads/2019/06/EP-activity-Report-2017.pdf> (accessed on 14 January 2024).
153. Gomez-Merchan, R.; Leñero-Bardallo, J.A.; López-Carmona, M.; Rodríguez-Vázquez, Á. A Low-Latency, Low-Power CMOS Sun Sensor for Attitude Calculation Using Photovoltaic Regime and On-Chip Centroid Computation. *IEEE Trans. Instrum. Meas.* **2023**, *72*, 2003412. [[CrossRef](#)]
154. Chang, Y.-K.; Kang, S.-J.; Lee, B.-H. High-Accuracy Image Centroiding Algorithm for CMOS-Based Digital Sun Sensors. In Proceedings of the 2007 IEEE Sensors, Atlanta, GA, USA, 28–31 October 2007. [[CrossRef](#)]
155. Romijn, J.; Vollebregt, S.; May, A.; Erlbacher, T.; van Zeijl, H.W.; Leijtens, J.; Zhang, G.; Sarro, P.M. Visible Blind Quadrant Sun Position Sensor in a Silicon Carbide Technology. In Proceedings of the 2022 IEEE 35th International Conference on Micro Electro Mechanical Systems Conference (MEMS), Tokyo, Japan, 9–13 January 2022. [[CrossRef](#)]
156. Romijn, J.; Vollebregt, S.; de Bie, V.G.; Middelburg, L.M.; El Mansouri, B.; van Zeijl, H.W.; May, A.; Erlbacher, T.; Leijtens, J.; Zhang, G.; et al. Microfabricated albedo insensitive sun position sensor system in silicon carbide with integrated 3D optics and CMOS electronics. *Sens. Actuators A Phys.* **2023**, *354*, 114268. [[CrossRef](#)]
157. Romijn, J.; Sanseven, S.; Zhang, G.; Vollebregt, S.; Sarro, P.M. Angle Sensitive Optical Sensor for Light Source Tracker Miniaturization. *IEEE Sens. Lett.* **2022**, *6*, 3501404. [[CrossRef](#)]
158. Koch, C.; Oehm, J.; Gornik, A. High precision optical angle measuring method applicable in standard CMOS technology. In Proceedings of the 2009 Proceedings of ESSCIRC (ESSCIRC), Athens, Greece, 14–18 September 2009. [[CrossRef](#)]

Disclaimer/Publisher’s Note: The statements, opinions and data contained in all publications are solely those of the individual author(s) and contributor(s) and not of MDPI and/or the editor(s). MDPI and/or the editor(s) disclaim responsibility for any injury to people or property resulting from any ideas, methods, instructions or products referred to in the content.